Université d'Ottawa · University of Ottawa

A Novel Method for the Determination of Single Crystal Elastic Constants Using Powder X-ray Diffraction

by

Weimin Hou

Thesis submitted to
the Faculty of Graduate and Postdoctoral Studies
of the University of Ottawa in partial fulfillment of the
requirements for the degree of M. Sc. in Physics

Abstract

The elastic properties of a material have long been a subject of interest in materials science and physics. Especially, a complete determination of the single crystal compliance and stiffness tensor is of great importance, as the single crystal elastic tensor provides a complete description of the elastic properties of a material.

There are numerous materials that are only available in polycrystalline form. Many of these polycrystalline materials are of great interest, such as the polycrystalline materials synthesized under high pressure conditions, for which the elastic properties under high pressure conditions are particularly important. However, traditional methods to measure the elastic constants apply only to single crystals.

Recently, Singh and co-workers have developed a method, using energy dispersive X-ray diffraction to measure the single crystal elastic constants of a material at elevated pressures, which, for the first time, enabled the single crystal elastic tensors of numerous polycrystalline samples to be determined.

Inspired by the energy dispersive X-ray diffraction method, we have undertaken to develop a novel method, using angle dispersive X-ray diffraction techniques combined with a two-dimensional X-ray recording area detector, to measure the single crystal elastic constants of powder samples. We have obtained important results that will enable the single crystal elastic constants of concerned material to be determined from Debye rings recorded on the X-ray recording image plate. In comparison to the energy

dispersive X-ray diffraction method, the angle dispersive X-ray diffraction method offers advantages, as we will demonstrate.

A Novel Method for the Determination of Single Crystal Elastic Constants Using Powder X-ray Diffraction

Weimin Hou

Recently, Singh and co-workers have developed a method, using energy dispersive X-ray diffraction to measure the single crystal elastic constants of a material at elevated pressures, which, for the first time, enabled the single crystal elastic tensors of numerous polycrystalline samples to be determined.

Inspired by the energy dispersive X-ray diffraction method, we have undertaken to develop a novel method, using angle dispersive X-ray diffraction techniques combined with a two-dimensional X-ray recording area detector, to measure the single crystal elastic constants of powder samples. We have obtained important results that will enable the single crystal elastic constants of concerned material to be determined from Debye rings recorded on the X-ray recording image plate. In comparison to the energy dispersive X-ray diffraction method, the angle dispersive X-ray diffraction method offers advantages, as we will demonstrate.

Table of Contents

List of Figures

List of Tables

ACKNOWLEDGMENTS

I am eternally grateful to my supervisor, Dr. S. Desgreniers, who helped guide me to this end, for his supervision, academic, financial, and moral support.

I wish to acknowledge the financial support of the University of Ottawa in the form of tuition fee waiver.

I am thankful to Dr. P. Piercy, Dr. Z. M. Stadnik, Dr. D. G. Rancourt, Dr. R. J. W. Hodgson and Dr. I. L'Heureux, for their help and support. Thanks are extended to all in the Department of Physics for their help on countless occasions.

I am also thankful to my friends M. Lee, P. Mercier, and J. P. Prevost, for their kind help.

Finally, I would like to thank all my family members, for their endless support, patience, and encouragement.

Statement of Originality

To the best of my knowledge, the method using angle dispersive X-ray diffraction techniques to measure the single crystal elastic constants of a polycrystalline sample, developed during the course of this thesis work for the fulfilment of the requirements for the Degree of M. Sc. in physics at University of Ottawa under the supervision of Dr. Serge Desgreniers is novel.

In addition, some work performed on RuO_2 and MnO_2 is not presented as part of this thesis. I have written several small programs, which greatly increase our productivity throughout this work.

Chapter 1. Introduction

1.1 Importance of the Determination of the Single Crystal Elastic Constants (SCEC)

The knowledge and understanding of the elastic properties of a material have long been a subject of interest in materials science and physics [1, 2]. The elastic properties of a material can be characterized either by macroscopic quantities, such as the bulk and shear moduli, or by microscopic quantities, such as the single crystal stiffness C_{ij} or compliance S_{ij} (referred to as single crystal elastic constants (SCEC) in this work). There are relationships between the macroscopic and the microscopic elastic quantities [1, 2].

The single crystal stiffness or compliance tensors provide a complete description of the elastic properties of a material, especially when the anisotropy of the elastic properties is concerned. For instance, the identification of the hardness of materials involves the measurement of both the bulk modulus and the shear modulus. Especially for the measurement of the shear modulus, which has been suggested to be a better indicator of the hardness of a material, a complete determination of the SCEC is required [3]. Moreover, information on single crystal elastic constants is essential for the understanding of atomic interactions, mechanical stability of solids, phase transformation mechanisms, material strength, and seismology.

Recently, in an effort to understand the Earth's interior, attempts at extracting single crystal elastic constants information from some iron-bearing materials have been

reported. Needless to say that the knowledge of the elasticity of geo-materials at very high pressures, such as the high density hexagonal close-packed phase iron (ε-Fe), is important for understanding of the reported seismic anisotropy and rotation of the Earth's inner core [4].

Developing a reliable method to determine the single crystal elastic constants, especially in a situation where a material is subjected to moderate and high pressures, has been the object of many reports [5-14].

1.2. Traditional Methods to Measure SCEC

By measuring the effect of pressure on the propagation of elastic waves in a material, the single crystal stiffness (or compliance) tensor components can be determined. Conventional measurements have been carried out using ultrasonic and Brillouin spectroscopic methods. These traditional methods are usually limited to measurements at low and moderate pressure and generally apply only to single crystals, especially when the anisotropic elastic properties of a material are of interest [15, 16].

As ultrasonic waves propagate in an elastic solid, an interaction between the ultrasonic waves and lattice vibrations occurs. By measuring the sound velocities and attenuations (energy losses) of the ultrasonic waves propagating through a solid, the elastic constants of the solid can be obtained [17]. This method (referred to as "ultrasonic method" in this work) is generally limited to pressures below 3 GPa for single crystal studies [18].

Using Brillouin spectroscopy, however, one is able to measure the velocities (or the energy) of the acoustic phonons (acoustic branches of the lattice vibrations) at elevated pressures. Information on the single crystal elastic constants can then be extracted. Brillouin spectroscopy can be carried out up to 25 GPa in a diamond anvil cell; it has, however, been successfully applied only to optically transparent single crystals under hydrostatic pressure conditions, provided by the best pressure transmitting media [16]. For materials that are not optically transparent, such as metals and semiconductors, Brillouin spectroscopy is difficult to apply or simply does not work.

There are numerous materials that are only available in a polycrystalline form, and hence are not suitable for the above two methods. For instance, materials in high-density phases synthesized at high pressure are generally obtained only as polycrystalline aggregates. As these high-density materials are usually possible candidates for novel superhard materials, their elastic properties, and especially the single crystal elastic constants, are of great interest. It is clear that more appropriate methods are needed to extract the microscopic single crystal elastic information from the polycrystalline samples. Recently, powder X-ray diffraction techniques have attracted extensive attention, for the purpose to determine the SCEC of materials [8, 12-14].

In the present work, we have undertaken to develop a method to determine the SCEC from powder X-ray diffraction of polycrystalline materials, namely, the angle dispersive X-ray diffraction method. The details of this method will be addressed in Chapter 4.

1.3. Advantages of Powder X-ray Diffraction Using Synchrotron Radiation

Powder X-ray diffraction is one of the most important, powerful, and widely used analytical techniques available to scientists [19]. Powder X-ray diffraction techniques are generally used to identify unknown materials by measuring the d-spacings of the diffracting planes of a concerned material. More importantly, powder X-ray diffraction techniques apply very well to those polycrystalline samples with grain sizes in the range of 5-10 μm, or even apply to samples with grain size well into the nanometer range [19]. Powder X-ray diffraction techniques provide the unique analytical tools for studying these numerous materials, which are only available in polycrystalline form.

With the use of synchrotron radiation and high-resolution X-ray detectors, X-ray diffraction patterns are nowadays recordable up to extreme pressure, in excess of 200 GPa [20]. Moreover, with the tunability of the wavelength (or the energy) of synchrotron radiation, X-ray diffraction techniques using synchrotron radiation become even more powerful in probing the structure parameters of materials.

By adjusting the wavelength (or the energy) of the incident X-ray beam to carry out X-ray diffraction away from the absorption edges of the concerned material, X-ray diffraction patterns with high signal-to-noise ratio and high quality can be acquired; using resonant X-ray diffraction techniques, elements with their X-ray diffraction atomic factors close to each other can be effectively discriminated [19]. Advantages associated with the synchrotron X-ray diffraction techniques make it feasible to probe the

microstructure information of a material, such as the stress and strain, up to very high pressure. As we will show, the determination of the SCEC is carried out under nonhydrostatic pressure conditions.

1.4. Measuring SCEC under Nonhydrostatic Compression

Placing a sample inside the diamond anvil cell (DAC, details are given in Chapter 2) along with a pressure-transmitting medium, a quasi-hydrostatic pressure environment can be kept up to very high pressure. Although measurements carried out under hydrostatic pressure are desirable in many situations, they cannot provide all the necessary information to determine all the elasticity tensor elements. On one hand, measurements carried out under hydrostatic pressure provides one independent equation for the cubic system and up to six equations for triclinic systems, while there are three elasticity tensor elements for cubic systems and twenty-one for triclinic systems to be determined [1, 2]. In other words, such measurements only account for approximately one third of all the equations required to determine the complete SCEC tensor.

On the other hand, X-ray diffraction patterns recorded under nonhydrostatic stress conditions contain a wealth of additional information in regards to the elasticity of a material, which is not available from the X-ray diffraction patterns recorded under hydrostatic pressure conditions. Under nonhydrostatic stress conditions, it is possible, in principle, to carry out a complete determination of all the single crystal elastic constants of a material, as we will show, if the symmetry is cubic.

Traditionally, lattice strain theories have been applied to correct systematic effects caused by nonhydrostatic stresses occurring at high pressure; the same theories are now used to help analyze more efficiently a nonhydrostatic stress state, for the purpose of the determination of the complete elasticity tensor. By intentionally loading a sample into a DAC without any pressure-transmitting medium, a uniaxial stress along the load direction is created and fully exploited.

1.5. Feasibility of Using Powder X-ray Diffraction to Determine SCEC

We now consider a powder sample loaded into a DAC and experiencing a uniaxial stress. Due to the completely random alignment of each crystallite of the powder sample, the orientation of each lattice plane normal of the polycrystalline sample, with respect to the DAC load direction, is completely random. Under a specific loading, the magnitude of the applied uniaxial stress is the same for all the crystallites inside the DAC, but the relative orientation of the uniaxial stress with respect to different diffracting plane normals is different. Therefore, the effect of the uniaxial stress on compressing different lattice planes is different, depending on their relative orientation.

X-ray diffraction must satisfy Bragg's law. According to Bragg's law, if the path of both the incident and the diffracted X-ray beam (we know this from the experimental setup) are known, then the orientation of the diffracting plane normal pertaining to the X-ray diffraction can be determined. This means that with a proper experimental setup, one

is able to select a group of diffracting planes, from which the X-ray diffraction patterns are recorded.

For instance, for the case of energy dispersive X-ray diffraction (EDXD, details in Chapter 2), where the wavelength of the incident X-ray beam is continuous and the X-ray diffraction angle 2θ is fixed, a collimator is placed in front of a detector to select a group of diffracted X-ray beams. Knowing the paths of both the incident and the diffracted X-ray beams, the orientation of the plane normals of the selected group of lattice planes can be determined. The angle between the load axis and the diffracting plane normal (referred to as ψ in this work) is then measured before an X-ray spectrum is recorded. The DAC then is rotated so that the angle ψ is changed. Again the new angle ψ is measured before another X-ray spectrum is taken (details are given in Chapter 4). The procedure can be repeated as many times as necessary so that all the situations corresponding to the different stress states, for which the relative orientation of the load axis and the diffracting plane normals are different, can be studied separately.

One can also increase the loading on a sample to change the magnitude of the stress, as the magnitude of the unaxial stress is more or less linearly proportional to the pressure on the sample [12, 13]. In this way, all the situations corresponding to the different diffracting planes (with different Miller indices) under different stress states (either the magnitude or the orientation or both are different) can be selected out and studied separately. Using powder X-ray diffraction techniques, one can actually take the advantage of the random alignment of the orientations of the crystallites, to extract the information on the single crystal elasticity tensor.

Based on this idea, Singh and co-workers have successfully determined the elasticity tensor components of ε-Fe (hexagonal phases) under nonhydrostatic compression up to 52 GPa [8]. Duffy and co-workers have measured the elasticity tensors of gold and rhenium up to 37 GPa [12]. For the first time, the determination of the single crystal elasticity tensors of metals at very high pressure has been possible.

1.6. Determination of SCEC Using Angle Dispersive X-ray Diffraction (ADXD)

Can one determine the SCEC more completely and accurately using angle dispersive X-ray diffraction (ADXD, details are given in Chapter 2) instead of using EDXD? This is the question we want to address in the present work. Detectors used for angle dispersive X-ray diffraction (usually area detectors) have a higher accuracy (resolution) than those used for energy dispersive X-ray diffraction. The higher resolution is crucial in this situation, as the changes in d-spacings (strains) resulting from stresses are very small [12]. Another advantage in using ADXD is that one can record all the information with a single measurement. Using the angle dispersive X-ray diffraction technique combined with a two-dimensional area detector (an image plate), complete Debye rings (traces arising from powder X-ray diffraction) can be recorded. Each Debye ring corresponds to a different set of Miller indices, and each point on a Debye ring corresponds to a different stress state (details are given in Chapter 4). Hence a wealth of information is found in the recorded Debye rings.

Obviously, each point on every Debye ring satisfies Bragg's law. Considering one specific point on a Debye ring recorded on the two-dimensional area detector (an image plate), the corresponding path of the incident X-ray beam can be determined from the experimental setup, as well as the path of the diffracted X-ray beam. Therefore one can retrace the information pertaining to the corresponding diffracting planes as done for the case of the energy dispersive X-ray diffraction method. Provided a uniaxial stress is applied and considering one specific point on a Debye ring, one is able to determine the relative orientation of the plane normal of the corresponding diffracting planes, with respect to the loading axis. We can then study the arising strains and further extract the elasticity tensor information.

If the direction of the stress applied to the sample is perpendicular to the incident X-ray beam, the Debye rings recorded on the two-dimensional area detector are mostly elongated along the direction parallel to the loading axis and mostly compressed in the direction perpendicular to the loading axis (in terms of the X-ray diffraction angle 2θ). In comparison, the Debye rings are perfect circles when there is no uniaxial stress applied (under hydrostatic pressure condition) or the direction of the applied uniaxial stress is parallel to the incident X-ray beam [21]. This is due to the fact that the applied stress has a different effect on compressing the spacing between the diffracting planes, depending on the relative orientation of the loading axis with respect to the diffracting plane normal, even when the Miller indices are identical.

The mathematical derivation of all the necessary equations to calculate the single crystal elastic compliance or stiffness tensor components for the angle dispersive X-ray diffraction method is more complicated than that for the energy dispersive X-ray

diffraction method (as the diffracting angle 2θ is fixed for EDXD). For the angle dispersive X-ray diffraction method, at least three different angles are involved and all of them are subjected to change in response to the different stress states. These three angles are, namely, the X-ray diffracting angle 2θ (Bragg angle), the azimuthal angle ϕ (along a given Debye ring), and the angle ψ, i.e., the angle between a diffracting plane normal and the loading axis.

Before the present work, the possibility to extract the information on the single crystal elastic constants using angle dispersive X-ray diffraction method was raised [22, 23]. However, problems arising were not resolved quantitatively and the proposed solutions were advanced only with some assumptions and approximations.

1.7. Purpose and Scope of This Thesis

In this thesis, we report a novel method to extract the single crystal elastic constants using the information found from angle dispersive X-ray diffraction method. Following the formalism elaborated for the energy dispersive X-ray diffraction, theoretical derivations have been carried out for angle dispersive X-ray diffraction, and important results have been obtained. Using our results, the single crystal elasticity information can be extracted using all the points on the distorted Debye rings recorded at high pressure. Experimental attempts have been made and the feasibility of the method has been proven.

In Chapter 2, basic aspects of high-pressure physics and powder X-ray diffraction techniques using synchrotron radiation are described. In Chapter 3, lattice strain theories

on the elastic strain and stress under nonhydrostatic compression conditions are presented. In Chapter 4, we will present a summary of using the EDXD method to determine the SCEC from powder X-ray diffraction patterns, and explain in detail how the novel method developed in this work, the ADXD method, is used to determine the SCEC of materials. In Chapter 5, we will present and discuss in detail some important results that we have derived for the ADXD method. Finally, we will summarize and give conclusions in Chapter 6.

Chapter 2. Experimental Techniques

In this Chapter, we review the techniques utilized to study polycrystalline samples under high pressure conditions by powder X-ray diffraction technique using synchrotron radiation. High pressure is generated using diamond anvil cells (DAC).

2.1 Generating and Measuring High Pressure

2.1.1 The Diamond Anvil Cell (DAC)

As shown in Figure 2.1, the diamond anvil cell (DAC) is basically composed of two opposing diamond anvils and a metallic gasket inserted between the flat culets (typically 300μm in diameter) of the two diamond anvils. Diamond is the ideal material for being an anvil because of its hardness and optical transparency. A tiny hole (70-100μm in diameter) is drilled right in the centre of an indentation left by the diamond anvils on the gasket, where a sample is loaded. Upon loading a sample, usually along with a pressure transmitting medium and a pressure gauge, is sealed inside the hole by the upper and lower diamond anvils; the hole in the gasket is usually referred to as the high pressure chamber. High pressure is generated by moving the two diamond anvils towards each other by mechanical or pneumatic means.

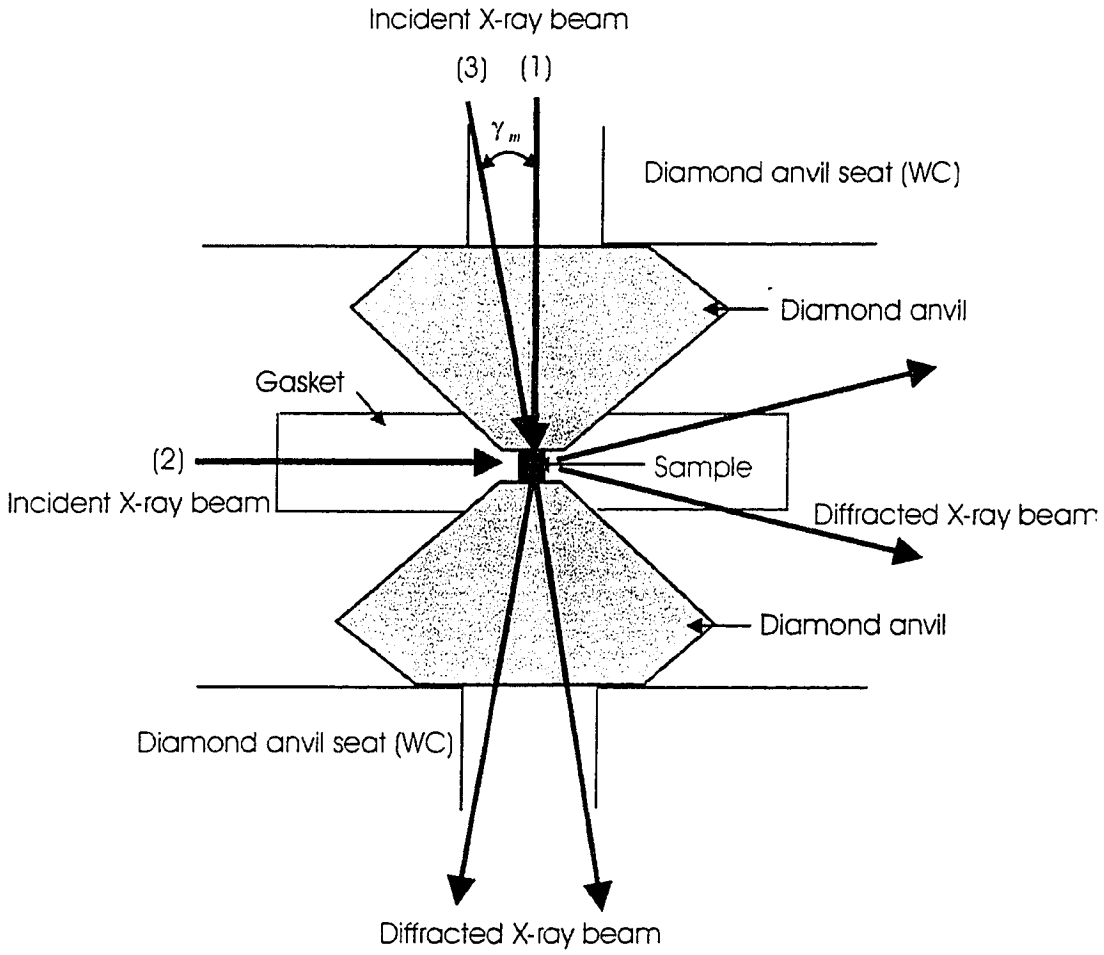

Figure 2.1 DAC structure. (1) Parallel geometry. (2) Perpendicular geometry. (3) Nearly parallel geometry.

The gasket material must be strong enough to hold the high pressure yet ductile to deform under load, therefore, it is usually pre-indented using the DAC before a hole is drilled, in order to increase its strength. For example, an initially 250 μm-thick gasket, made out of hardened stainless steel (AISI T301), is pre-indented to approximately 50-70 μm.

In order to generate a pressure environment as hydrostatic as possible, a pressure transmitting medium is used to fill the high pressure chamber before it is closed. Generally, either a 4:1 mixture of methanol and ethanol or silicone oil is used to transmit the pressure hydrostatically to the sample and to prevent the high pressure chamber from collapsing under loading.

For the hydrostatic pressure studies, the direction of the incident X-ray beam coincides with the load axis (the direction in which the pressure is applied), i.e., the incident X-ray beam passes through the upper diamond, illuminates the sample, and the diffracted and undiffracted beams pass through the lower diamond (shown as path (1) in Figure 2.1). This configuration is referred to as the parallel geometry in this work. In this case, as the X-ray beams do not interfere with the gasket (passing right through the high pressure chamber in the gasket), the gasket need not be X-ray transparent in the parallel geometry. Therefore, high atomic number materials like hardened stainless steel can be used as the gasket materials. The description above refers to a conventional DAC for hydrostatic pressure studies.

In the present work, we are focusing on the determination of single crystal elastic constants (SCEC) of a material. The study of a material under hydrostatic pressure conditions cannot provide all the needed results to estimate the SCEC [1, 2], therefore a nonhydrostatic pressure environment is intentionally created, by loading the sample without any pressure transmitting medium inside the high pressure chamber.

Modifications are made to the conventional DAC, in order to extract the information on the single crystal elastic constants from the X-ray diffraction pattern. In this case, the incident X-ray beam is set perpendicularly to the load axis, which is shown as path (2) in

Figure 2.1, and both the incident and the diffracted X-ray beams pass through the gasket. This configuration is referred to as the perpendicular geometry in this work. The complete justification as to why the perpendicular geometry is needed will be discussed in Chapter 4. In this case, the gasket material must be transparent to hard X-rays, in order to record the X-ray diffraction pattern from the sample. High-strength Be is used as the gasket material to fulfill this purpose.

As shown in Figure 2.1 (path (3)), γ_m is the maximum angle allowed by the DAC to pass the X-ray beam through both the upper and lower diamond anvil, without interfering with the gasket and the opening of the DAC. In this work, it is referred to as the nearly parallel geometry. If γ_m is large enough, it is possible to determine the SCEC using the nearly parallel geometry without having the X-ray beam going through the gasket as for the case of the perpendicular geometry [14].

2.1.2 Pressure Measurements

In order to determine the pressure inside the high pressure chamber, a small quantity of powdered metal with a well-known equation of state (EOS) is usually placed along with the sample inside the high pressure chamber. The powdered metal with a well-known EOS serves as the pressure gauge.

Ideally, a pressure gauge must first be stable as a function of pressure over the pressure range of interest, i.e., there is no phase transition occurring for the pressure gauge over the pressure range of concern. Secondly, usually the pressure gauge must

have a high symmetry crystalline structure. Because the lower symmetry crystalline structure results in more diffraction lines in the X-ray diffraction pattern, which might overlap with the X-ray diffraction lines of the sample under study. Depending on the angle of the X-ray diffraction lines of the sample, a pressure gauge is chosen so that its X-ray diffraction lines interfere the least with the sample lines.

Under loading, the pressure gauge, along with the sample, is subjected to compression. Based on the corresponding volume of a unit cell of the pressure gauge determined from the X-ray diffraction pattern, the pressure is determined using a parameterized equation of state like the third-order Birch-Murnaghan equation [2, 24]:

$$P = \frac{3}{2} B_0 \left[\left(\frac{V_0}{V} \right)^{\frac{7}{3}} - \left(\frac{V_0}{V} \right)^{\frac{5}{3}} \right] \left\{ 1 + \frac{3}{4} \left(B_0' - 4 \right) \left[\left(\frac{V_0}{V} \right)^{\frac{2}{3}} - 1 \right] \right\}, \tag{2.1}$$

where B_0 is the bulk modulus and B_0' is the pressure derivative of the bulk modulus extrapolated at ambient pressure. B_0 and B_0' are known parameters for the pressure gauge. Au, Pt, Mo, and Cu are metals commonly used as pressure gauges.

Due to the optical transparency of the diamond, optical methods can be used to determine the pressure as well. In this case, an optical pressure gauge, such as ruby ($Al_2O_3:Cr^{3+}$), is placed in the high pressure chamber with a sample. Ruby has two characteristic luminescence peaks (known as R-lines centred at 692.7 and 694.25 nm at ambient condition), corresponding to the transitions between the electronic states of the Cr^{3+} impurities in the Al_2O_3 lattice. These two characteristic luminescence peaks shift towards longer wavelength as the pressure increases, due to the slight modification of the electronic states arising from the applied pressure. Based on the shift of these two

characteristic luminescence peaks of ruby, the corresponding quasi-hydrostatic pressure is determined according to [25]:

$$P(GPa) = 380.8\left[\left(\frac{\lambda_0 + \Delta\lambda}{\lambda_0}\right)^5 - 1\right], \tag{2.2}$$

where λ_0 is 694.25 nm, and $\Delta\lambda$ is the shift of the characteristic luminescence peaks recorded at pressure P.

As the ruby chips are in the form of single crystal, usually they would not have diffraction lines showing up in the powder X-ray diffraction pattern. Hence no interference with the X-ray diffraction lines from the sample is expected. This is an advantage of using an optical pressure gauge. The disadvantage is that an optical spectroscopy system is required to record the luminescence.

2.2 Powder X-ray Diffraction

2.2.1 General Description

Powder X-ray diffraction is one of the most important, powerful, and widely used analytical techniques available to scientists [19]. Using the Bragg's Law

$$2d_{hkl}\sin\theta = n\lambda, \tag{2.3}$$

where λ is the wavelength of the incident X-ray beam, 2θ is the X-ray diffraction angle, and n is the order of the diffraction, d-spacings of concerned materials (d_{hkl}) are determined. Based on the structure parameters determined by the X-ray diffraction,

unknown materials can be identified. Powder X-ray diffraction data can be used to do the refinement of crystal structure as well [19].

There are numerous materials only available in polycrystalline form. Especially, high-density materials synthesized under high pressure are generally obtained in the polycrystalline form. In this work, all the calculations and derivations apply only to polycrystalline samples.

In comparison to single crystal X-ray diffraction, which produces a spot for a specific diffraction condition, powder X-ray diffraction produces a cone for a specific diffraction condition satisfying Bragg's law, due to the completely random orientations of the numerous crystallites ($\sim 10^6$ crystallites/cm^2) in the powder sample [19] (provided the incident X-ray beam is monochromatic).

A conventional X-ray source has disadvantages due to its low brilliance, non-tunability, and relative high beam divergence. Moreover, the radiation is composed of the $K\alpha_1$-$K\alpha_2$ doublet, with relative intensities in the ratio 2:1. This structured wavelength distribution limited progress in a number of powder X-ray diffraction applications, particularly for materials having low and intermediate symmetry. In this work, as the microstructure information such as strain and stress is of interest, all experiments are carried out using synchrotron radiation.

Synchrotron radiation offers great advantages: high brilliance, extreme parallelism of the beam, tunability of wavelength (highly monochromatic beam is achievable), and a total linear polarization of the beam. To determine the SCEC of a material at high pressure, as the X-ray beam passes through the gasket, the wavelength of the incident X-ray beam needs to be adjusted, to minimize the absorption by the gasket material. In

some cases, the resonant X-ray diffraction technique is needed, to obtain a high quality X-ray diffraction image. Resonant X-ray diffraction can only be achieved using synchrotron radiation.

For the powder X-ray diffraction techniques using synchrotron radiation, two types of experimental setups are possible: angle dispersive X-ray diffraction (ADXD), in which monochromatic radiation is used, and energy dispersive X-ray diffraction (EDXD), for which "white" or polychromatic radiation is used.

2.2.2 Energy Dispersive X-ray Diffraction (EDXD)

Figure 2.2 illustrates the schematic experimental setup for the energy dispersive X-ray diffraction technique (EDXD). For the EDXD technique, the energy, or the wavelength, of the X-ray beam has a continuous distribution.

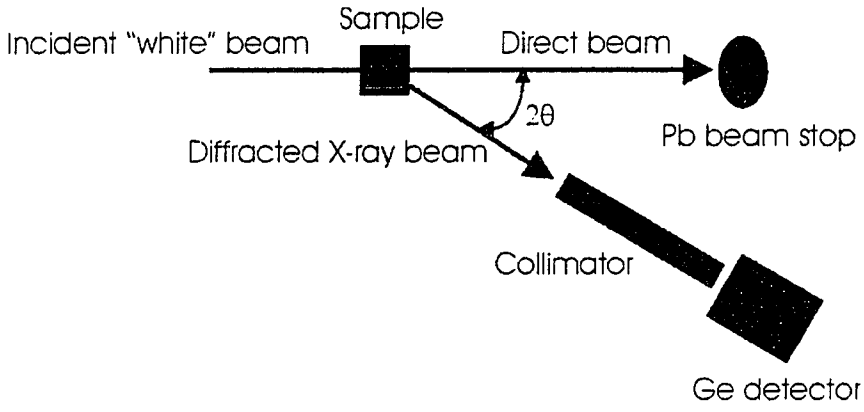

Figure 2.2. The experimental setup for the energy dispersive X-ray diffraction (EDXD).

Therefore, for a powder sample, the diffracted X-ray beam goes everywhere in the three-dimensional space. By placing a slit collimator in front of an energy-resolving detector (an intrinsic Ge detector), only those diffracted X-ray beams having an angle 2θ with respect to the direct beam (undiffracted beam) are selected and recorded by the Ge detector. In this way, the X-ray diffraction angle 2θ for the EDXD is fixed. Note that all the lattice planes pertaining to the structure of the concerned material contribute to the diffraction recorded by the Ge detector.

As

$$E = \frac{hc}{\lambda}, \tag{2.4}$$

a variation of Bragg's law is obtained for the EDXD:

$$Ed = \frac{hc}{2\sin\theta}, \tag{2.5}$$

where Ed is constant, as θ is fixed. Ed or the angle θ is calibrated using the X-ray diffraction spectra of a known material. After Ed is calibrated, i.e., the angle θ is known, the d-spacing of a lattice plane (hkl) is determined by the energy of its corresponding diffraction peak E_{hkl}:

$$d_{hkl} = \frac{Ed}{E_{hkl}}. \tag{2.6}$$

In this way, one is able to obtain X-ray diffraction patterns using the EDXD.

2.2.3 Angle Dispersive X-ray Diffraction (ADXD)

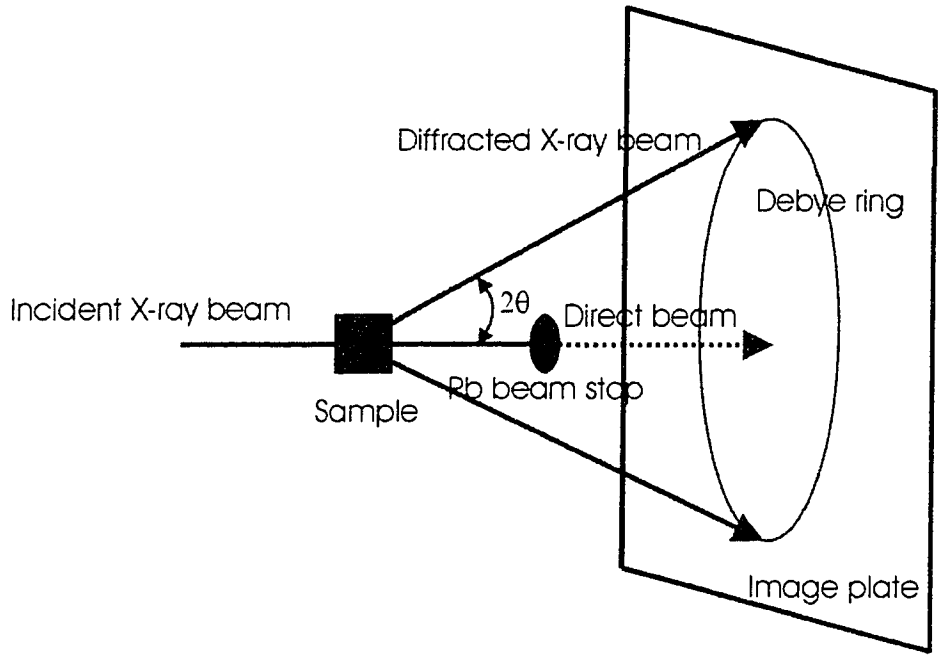

Figure 2.3. The experimental setup for the angle dispersive X-ray diffraction (ADXD).

Figure 2.3 shows the schematic diagram of the experimental setup for the angle dispersive X-ray diffraction (ADXD) techniques. In comparison to the energy dispersive X-ray diffraction, the incident X-ray beam is monochromatic for the angle dispersive X-ray diffraction. An X-ray recording image plate with a size of 200×250 mm^2, is used as the detector for the ADXD. The image plate is generally placed perpendicularly to the incident X-ray beam, to record the Debye rings created by the powder X-ray diffraction. A small lead beam stop is used to avoid that the undiffracted X-ray beam (direct beam) to saturates the image plate, yet not to absorb the beam completely. The spot where the

direct beam hits the image plate is used to locate the position of the incident X-ray beam, from which the 2θ angle is then measured.

The image plate is essentially a phosphor-coated plate, which is able to temporarily store the information corresponding to the complete X-ray diffraction image. The phosphor is put in an excited state when illuminated by the X-rays. After the measurement, a FUJI BAS2000 scanner is used to retrieve the information of the complete X-ray diffraction pattern, where a laser is used to illuminate the image plate pixel by pixel, and the induced luminescence is recorded to build a complete image of the Debye rings.

For hydrostatic pressure studies, where the parallel geometry is used, the recorded Debye rings are perfect circles. The image is then converted into a 2θ profile using SimPA [26]. In the work to determine the SCEC, where the experiments are carried out under nonhydrostatic pressure conditions, the perpendicular geometry is used, and the recorded Debye rings are distorted from being perfect circles, due to the strains experienced by the powder sample [21]. In this case, the image cannot be integrated into a 2θ profile. The diffraction angle 2θ and the azimuthal angle ϕ are read directly from the image using SimPA (details is given in Chapter 4).

For the ADXD method, a precise measurement of the sample-to-plate distance is required. Usually, two spectra of a known material are taken at different sample-to-plate distances (the image plate is placed at two positions after the DAC along the direct beam), and the distance between the two positions of the image plate is precisely measured. In this way, both of these two sample-to-plate distances can be determined

precisely [27]. The image plate is fixed at one of these two positions during the course of an experiment, unless the position of the DAC is changed.

In comparison to the EDXD, the intrinsic resolution of the ADXD method is roughly an order of magnitude better than that of the EDXD method. In this work, as we focus on the microstructure information, such as strain and stress, an image with a high resolution is very important for the following analysis process. Another advantage for the ADXD method is that complete Debye rings are recorded for study. As we will see in Chapter 4, strains at different points along the Debye rings provide a wealth of information to determine the single crystal elastic constants.

Chapter 3. Elastic Strains Under Nonhydrostatic Compression

In this Chapter, the cubic system under the Reuss limit is taken as an example to carry out the calculations of the elastic strains under nonhydrostatic compression.

3.1. The Stress State Inside the Diamond Anvil Cell (DAC)

Under hydrostatic pressure, the sample inside the diamond anvil cell (DAC) experiences isostress from all the directions. As shown in Figure 3.1, if we set up an orthogonal right-handed coordinate system (X, Y, Z) such that the X-axis and Y-axis are parallel to the anvil culet and Z-axis is along the load direction, and the origin is located at the center of the diamond anvil cell (this coordinate system is referred to as the load coordinate system in this work), then the stress state tensor is given by

$$\sigma = \begin{pmatrix} \sigma_p & 0 & 0 \\ 0 & \sigma_p & 0 \\ 0 & 0 & \sigma_p \end{pmatrix}, \tag{3.1}$$

where σ_p is the hydrostatic pressure and it is isotropic in this case.

Under very high pressure, or when there is no pressure-transmitting medium inside the diamond anvil cell, a sample inside the diamond anvil cell experiences nonhydrostatic pressure conditions. In this case, the stress component along the load direction (Z-axis),

namely, σ_3, is greater than those along the radial direction (along X-axis or Y-axis), namely, σ_1 and σ_2, respectively. Generally, the stress component along the radial direction is approximately uniform. Therefore σ_1 and σ_2 are equal to each other.

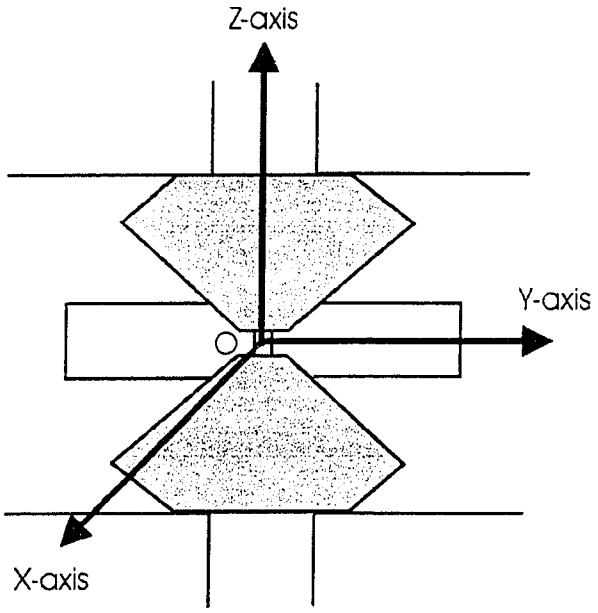

Figure 3.1 The load coordinate system (X, Y, Z). Z-axis is along the load direction, X-axis and Y-axis are parallel to the diamond anvil culets, the origin is located at the center of the DAC.

In the load coordinate system as shown in Figure 3.1, the stress state at the center of the DAC is described by the following tensor:

$$\sigma = \begin{pmatrix} \sigma_1 & 0 & 0 \\ 0 & \sigma_1 & 0 \\ 0 & 0 & \sigma_3 \end{pmatrix} = \begin{pmatrix} \sigma_p & 0 & 0 \\ 0 & \sigma_p & 0 \\ 0 & 0 & \sigma_p \end{pmatrix} + \begin{pmatrix} -t/3 & 0 & 0 \\ 0 & -t/3 & 0 \\ 0 & 0 & 2t/3 \end{pmatrix}, \tag{3.2}$$

where σ_3 is the stress component in the load direction, σ_1 is the stress component in the radial direction (along either X- or Y-axis).

The first term on the right-hand side of equation (3.2) corresponds to the hydrostatic pressure tensor as described in equation (3.1), with

$$\sigma_p = (\sigma_1 + \sigma_1 + \sigma_3)/3 \ . \tag{3.3}$$

The second term of equation (3.2) is the deviatoric stress tensor, with

$$t \equiv \sigma_3 - \sigma_1, \tag{3.4}$$

where t is the difference between the maximum (σ_3) and the minimum (σ_1) stress components, and is usually referred to as the uniaxial stress component (USC).

It should be noted that so far only the stress state at the center inside the DAC has been discussed. In a real situation, there is a stress gradient existing inside the DAC, especially along the radial direction. The stress state should be modified a little if the actual position is off the center of the DAC. However, as both the thickness of the sample and the size of the hole in the gasket, i.e., the high pressure chamber, are smaller compared to the size of the diamond culets, equation (3.2) is regarded as a good description of the stress state everywhere inside the diamond anvil cell, not necessarily limited to the center of the DAC. In other words, the pressure distribution is assumed uniform inside the high pressure chamber for both hydrostatic and nonhydrostatic conditions.

Using equation (3.2) to describe the stress state inside the DAC, the isostress model (Reuss limit) [28] has actually been used to model the elastic behavior of a sample under compression. In other words, all the crystallites of a powder sample inside the DAC have

been assumed to experience the same stress. It should be noted that there is also another model, namely, the isostrain model (Voigt limit) [29], used to describe the elastic behavior of a solid sample. The Voigt limit will be discussed in Section 3.4. Unless indicated specifically, all the calculations in this work are carried out under the Reuss limit.

Measurements carried out under hydrostatic pressure cannot provide all the information necessary to determine the elasticity tensor elements. However, a sample under nonhydrostatic compression yields additional information regarding the single crystal elastic constants, which makes it possible to determine completely all the single-crystal elastic constants. Traditionally, lattice strain theories have been applied to correct the systematic effects caused by nonhydrostatic stresses under high pressure. In this work, these theories help the understanding of a nonhydrostatic stress state, and the determination of the elasticity tensor of a material [5-12].

Following the theories developed by Singh [5-9], theoretical calculations are carried out in the following sections, to extract information on the single crystal elastic constants for the cubic system from the distortion due to nonhydrostatic compression.

3.2. Definition of the Three Coordinate Systems

In this Section, the cubic system is taken as an example to calculate the strains under the nonhydrostatic stress state, as described by equation (3.2) (under the Reuss limit).

First, three orthogonal coordinate systems need to be defined, which are termed in this work as (1) crystallographic coordinate (X", Y", Z"), (2) diffracting plane coordinate (X', Y', Z'), and (3) load coordinate (X, Y, Z) systems, respectively.

As shown in Figure 3.2, the crystallographic coordinate system takes the crystallographic axes (a, b, c) as the coordinate system's axes (X", Y", Z").

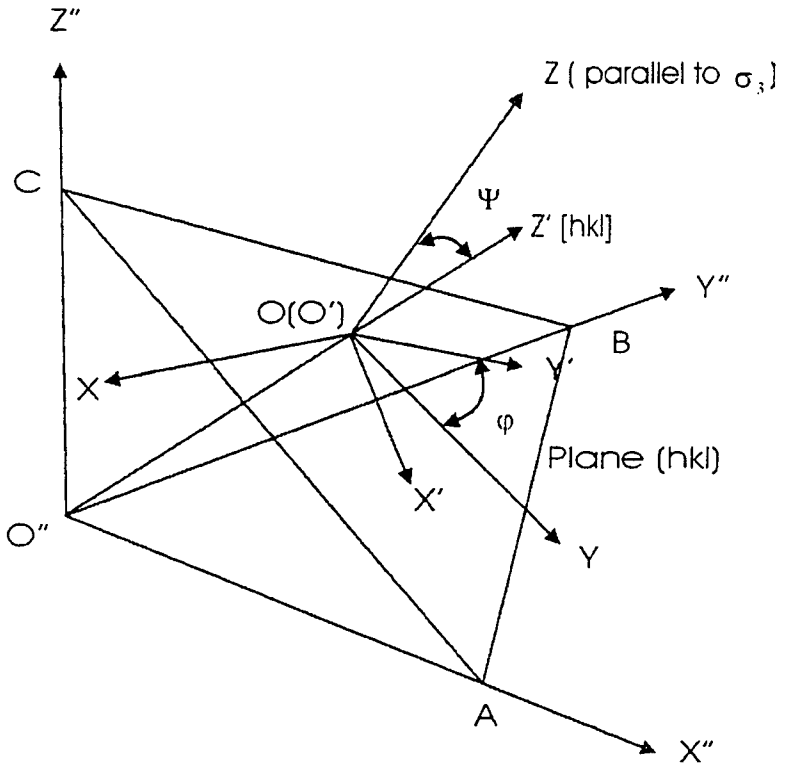

Figure 3.2 Relative orientations of the three relevant coordinate systems. (1) Crystallographic coordinate (X", Y", Z"). (2) Diffracting plane coordinate (X', Y', Z'). (3) Load coordinate (X, Y, Z).

Also shown in Figure 3.2, plane ABC is a diffracting plane with Miller indices *hkl*. The diffracting plane coordinate is set up so that the diffracting plane normal O"O' ([hkl])

is chosen as Z′-axis and O′A is chosen as X′-axis. Y′-axis is chosen to complete the orthogonal diffracting plane coordinate system.

The load coordinate is set up in the same way as described in Section 3.1 (refer to Figure 3.1), with the stress component σ_3 along Z-axis. As shown in Figure 3.2, the Y-axis lies in the diffracting plane ABC and makes an angle φ with respect to the Y'-axis and the Z-axis makes an angle ψ with respect to the Z'-axis. The X-axis is chosen (obviously not lying on the diffracting plane ABC) so as to complete the orthogonal coordinate system. It is noted that the Y-axis is perpendicular to both the Z and Z′-axes.

Using the three coordinate systems defined above, one can determine the relative orientations of the crystallographic axes, the diffracting plane normal, and the load axis. In the following section, the strains experienced by a sample under the nonhydrostatic compression are derived, based on the three coordinate systems defined above.

3.3. Strains under Nonhydrostatic Compression

In the crystallographic coordinate system (X", Y", Z"), the strain and stress tensors are related by [1]

$$\varepsilon''_{ij} = S_{ijkl}\sigma''_{kl} \qquad (i, j, k, l = 1, 2, 3), \tag{3.5}$$

where S_{ijkl} represent the fourth-rank elastic compliance tensor components and σ''_{kl} is given in two-suffix notation [1]. Note that the Einstein summation convention applies to equation (3.5) and all the subsequent equations. Equation (3.5) can be rewritten as

$$\varepsilon''_{m} = S_{mn}\sigma''_{n} \qquad (m, n = 1, 2, 3, 4, 5, 6), \tag{3.6}$$

where S_{mn} is a second-rank tensor and σ_n'' is given in single-suffix notation [1]. Recall the nonhydrostatic stresses discussed in section 3.1, σ_1, σ_2, and σ_3, are defined as the three stress components, for which the single-suffix notation is actually used. For the cubic system, the relations between the two-suffix notation and the single-suffix notation are as follows [1]:

$$\begin{aligned} &\sigma_{11} = \sigma_1, \quad \sigma_{22} = \sigma_2, \quad \sigma_{33} = \sigma_3, \\ &\sigma_{12} = \sigma_6, \quad \sigma_{13} = \sigma_5, \quad \sigma_{23} = \sigma_4. \end{aligned} \tag{3.7}$$

Note that σ_1, σ_2, and σ_3 are given in the load coordinate (X, Y, Z) system. In order to calculate the strains in the crystallographic coordinate system using equation (3.6) (or equation (3.5)), the stress components σ_1, σ_2 and σ_3 given in the load coordinate (X, Y, Z) system need to be converted into σ_n'' in the crystallographic coordinate (X", Y", Z") system. This can be carried out by the following two successive transformations:

$$\begin{aligned} \sigma_{ij}' &= a_{ik} a_{jl} \sigma_{kl}, \\ \sigma_{ij}'' &= b_{ik} b_{jl} \sigma_{kl}'. \end{aligned} \tag{3.8}$$

The quantity a_{ij} denotes the matrix of the cosines of the angles that the axes of the diffracting plane coordinate (X', Y', Z') system make with respect to those of the load coordinate (X, Y, Z) system. Similarly, b_{ij} denotes the matrix of cosines of the angles that the axes of the crystallographic coordinate (X", Y", Z") system make with respect to those of the diffracting plane coordinate (X', Y', Z') system.

Based on the three coordinate systems defined in Section 3.2 and following Singh [5], a_{ij} and b_{ij} are given by

$$a_{ij} = \begin{array}{c} \\ X' \\ Y' \\ Z' \end{array} \begin{array}{c} X \\ \cos\varphi\cos\psi \\ \sin\varphi\cos\psi \\ -\sin\psi \end{array} \begin{array}{c} Y \\ -\sin\varphi \\ \cos\varphi \\ 0 \end{array} \begin{array}{c} Z \\ \cos\varphi\sin\psi \\ \sin\varphi\sin\psi \\ \cos\psi \end{array} \tag{3.9}$$

and

$$b_{ij} = \begin{array}{c} \\ X'' \\ Y'' \\ Z'' \end{array} \begin{array}{c} X' \\ \frac{N}{M} \\ -\frac{hk}{MN} \\ -\frac{hl}{MN} \end{array} \begin{array}{c} Y' \\ 0 \\ \frac{l}{N} \\ -\frac{k}{N} \end{array} \begin{array}{c} Z' \\ \frac{h}{M} \\ \frac{k}{M} \\ \frac{l}{M} \end{array}, \tag{3.10}$$

respectively, where $M = \sqrt{h^2 + k^2 + l^2}$ and $N = \sqrt{k^2 + l^2}$.

After carrying out the two successive transformations according to equation (3.8), one gets the corresponding stress components σ''_{ij} in the crystallographic coordinate (X", Y", Z") system, in terms of the applied stress components σ_1, σ_2, and σ_3 in the load coordinate (X, Y, Z) system.

If a completely random orientation of the crystallites in the powder sample is assumed, then all terms involving the angle φ are averaged out according to $\langle\cos\varphi\rangle = \langle\sin\varphi\rangle = 0$ and $\langle\cos^2\varphi\rangle = \langle\sin^2\varphi\rangle = ½$ [5]. Therefore, the expressions of the stress components σ''_{ij} given in the crystallographic coordinate (X", Y", Z") system do not involve the angle φ. This assumption greatly simplifies the following calculations. It should be remembered that all the following calculations and results apply to powder samples only.

The stress components σ''_{ij} in the crystallographic coordinate system are given as follows:

$$\sigma_{11}'' = \frac{\sigma_1}{2M^2}[M^2 + h^2\sin^2\psi + (-h^2 + k^2 + l^2)\cos^2\psi]$$
$$+ \frac{\sigma_3}{2M^2}[M^2 - h^2\sin^2\psi - (-h^2 + k^2 + l^2)\cos^2\psi], \quad (3.11a)$$

$$\sigma_{22}'' = \frac{\sigma_1}{2M^2}[M^2 + k^2\sin^2\psi + (h^2 - k^2 + l^2)\cos^2\psi]$$
$$+ \frac{\sigma_3}{2M^2}[M^2 - k^2\sin^2\psi - (h^2 - k^2 + l^2)\cos^2\psi], \quad (3.11b)$$

$$\sigma_{33}'' = \frac{\sigma_1}{2M^2}[M^2 + l^2\sin^2\psi + (h^2 + k^2 - l^2)\cos^2\psi]$$
$$+ \frac{\sigma_3}{2M^2}[M^2 - l^2\sin^2\psi - (h^2 + k^2 - l^2)\cos^2\psi], \quad (3.11c)$$

$$\sigma_{12}'' = -\frac{hk}{2M^2}(\sigma_3 - \sigma_1)(1 - 3\cos^2\psi), \quad (3.11d)$$

$$\sigma_{13}'' = -\frac{hl}{2M^2}(\sigma_3 - \sigma_1)(1 - 3\cos^2\psi), \quad (3.11e)$$

$$\sigma_{23}'' = -\frac{kl}{2M^2}(\sigma_3 - \sigma_1)(1 - 3\cos^2\psi). \quad (3.11f)$$

Substituting equation (3.11) into equation (3.5) (or equation (3.6)), one obtains the elastic strain components ε_{ij}'' in the crystallographic coordinate system. As equation (3.5) (or equation (3.6)), which describes the relationship between the strains and the stresses, holds only in the crystallographic coordinate system, the stress components given in the load coordinate system must be converted into those given in the crystallographic coordinate system.

X-ray diffraction provides, using Bragg's law, the d-spacings of a material. By measuring the d-spacing of a specific diffracting plane under different compression conditions, one is able to determine the elastic strain of the concerned diffracting plane (along the diffracting plane normal). Based on the three coordinate systems defined above, the elastic strain along the diffracting plane normal is ε'_{33}, in the diffracting plane coordinate (X', Y', Z') system.

ε'_{33}, the elastic strain component along the diffracting plane normal in the diffracting plane coordinate system, and ε''_{ij}, the elastic strain components in the crystallographic coordinate system, are related by [1]

$$\varepsilon'_{33} = \varepsilon''_{ij} l_i l_j \qquad (i, j = 1, 2, 3), \tag{3.12}$$

where l_1, l_2, and l_3 represent the cosines of the angles that Z'-axis makes with X"-, Y"- and Z"-axis, respectively. By carrying out equation (3.12), one obtains the net strains along the Z'-axis in the diffracting plane coordinate system (X', Y', Z') due to all the strains in the crystallographic coordinate system (X", Y", Z").

By carrying out all the above calculations, we are able to find the relationships between the applied stress components in the load coordinate system, the corresponding elastic strain components in the diffracting plane coordinate system, and the elastic compliances of the concerned material, which are given in the crystallographic coordinate system. As both the applied stress components and the elastic strain along the diffracting plane normal can be determined by experimental techniques (details are given in Chapter 4), one is able to determine the complete set of elastic constants of the concerned material.

Under the Reuss limit (isostress model, the stress is identical in all direction) and for the cubic system, ε'_{33}, the strain along the diffracting plane normal, due to nonhydrostatic pressure as described by equation (3.2), can be written as [5, 6]

$$\varepsilon'_{33} = \varepsilon^{p} + \Delta\varepsilon^{d} \tag{3.13}$$

where

$$\varepsilon^{p} = (S_{11} + 2S_{12})\sigma_{p}, \tag{3.14}$$

$$\Delta\varepsilon^{d} = -\left(\frac{t}{3}\right)(1 - 3\cos^{2}\psi\ )(S_{11} - S_{12} - 3S\Gamma), \tag{3.15}$$

with

$$S = (S_{11} - S_{12} - S_{44}/2) \tag{3.16}$$

and

$$\Gamma = (h^{2}k^{2} + k^{2}l^{2} + l^{2}h^{2})/(h^{2} + k^{2} + l^{2})^{2}. \tag{3.17}$$

Γ is usually termed as the geometry factor, which is a function of *hkl*. ε^{p} is the elastic strain due to the corresponding hydrostatic pressure and $\Delta\varepsilon^{d}$ is the additional elastic strain introduced by deviatoric shear stresses.

Once the expression of the strain along the diffracting plane normal, ε'_{33}, is derived in terms of elastic compliances S_{ij} and applied stress components σ_1, σ_2 and σ_3, the coordinate systems need no longer be considered in the following calculations. For convenience, equation (3.13) is rewritten as

$$\varepsilon_{hkl}^{p+d} = \varepsilon^{p} + \Delta\varepsilon_{hkl}^{d}\ . \tag{3.18}$$

The subscript *hkl* indicates that the quantities ε_{hkl}^{p+d} and $\Delta\varepsilon_{hkl}^{d}$ are *hkl*-dependent. The superscripts *p* and *d* refer to the corresponding hydrostatic pressure and deviatoric stress, respectively.

As

$$\varepsilon_{hkl}^{p+d} = \varepsilon^{p} + \Delta\varepsilon_{hkl}^{d} = \frac{d_{hkl}^{p+d} - d_{hkl}^{o}}{d_{hkl}^{o}}, \tag{3.19}$$

where d_{hkl}^{p+d} and d_{hkl}^{0} are the d-spacings of lattice plane (hkl) under nonhydrostatic compression and ambient pressure, respectively, the expression for the d-spacings in terms of the applied stress components and the elastic compliances is finally obtained [8]:

$$d_{hkl}^{p+d} = d_{hkl}^{p}[1 + (1 - 3\cos^2\psi\ )Q(hkl)]. \tag{3.20}$$

Under the Reuss limit (isostress) for the cubic system, we have

$$Q(hkl) = (\frac{t}{3})\frac{1}{2G_R(hkl)} = (\frac{t}{3})(S_{11} - S_{12} - 3S\Gamma), \tag{3.21}$$

where $G_R(hkl)$ is the shear modulus under the Reuss limit:

$$[2G_R(hkl)]^{-1} = S_{11} - S_{12} - 3S\Gamma. \tag{3.22}$$

3.4 Under the Voigt Limit

Note that so far all calculations have been carried out under the Reuss limit. The calculations can be carried out as well under the Voigt limit (isostrain model), where the strains along all directions are the same. Under the Voigt limit, we have [12, 13]

$$\varepsilon_{hkl}^{p+d} = \varepsilon^{p} + \Delta\varepsilon_{i}^{d}, \tag{3.23}$$

where

$$\Delta\varepsilon_{1'}^{d} = -\left(\frac{5t}{6}\right)(1-3\cos^2\psi\ )\frac{(S_{11}-S_{12})S_{44}}{3(S_{11}-S_{12})+S_{44}}. \tag{3.24}$$

In comparison to equation (3.15), equation (3.24) does not involve the Miller indices *hkl*, which indicates that the strains under the Voigt limit are isotropic and hkl-independent. This is the very reason for which the Voigt limit is also termed the isostrain model. Under the Voigt limit, the d-spacings are written as

$$d_{hkl}^{p+d} = d_{hkl}^{p}[1+(1-3\cos^2\psi\ )Q_{1'}]. \tag{3.25}$$

In this case,

$$Q_{1'} = (\frac{t}{3})\frac{1}{2G_{1'}} = (\frac{5t}{6})\frac{(S_{11}-S_{12})S_{44}}{3(S_{11}-S_{12})+S_{44}}, \tag{3.26}$$

where G_V is the shear modulus under the Voigt limit:

$$(2G_{1'})^{-1} = (\frac{5}{2})\frac{(S_{11}-S_{12})S_{44}}{3(S_{11}-S_{12})+S_{44}}. \tag{3.27}$$

Note that the only difference between equations (3.25) and (3.20) is that Q(hkl) in equation (3.20) is replaced by Q_V in equation (3.25).

In a real situation, the d-spacings are best described by a combination of both the Reuss Limit and Voigt limit as [12, 13]

$$d_{hkl}^{p+d} = d_{hkl}^{p}[1+(1-3\cos^2\psi\ )Q_{R+1'}(hkl)], \tag{3.28}$$

where

$$Q_{R+1'}(hkl) = \frac{t}{3}\left[\frac{\alpha}{2G_R(hkl)}+\frac{1-\alpha}{2G_{1'}}\right]. \tag{3.29}$$

The parameter α, which varies from 0 to 1, indicates how much each model contributes to the total strains. For instance, if α equals 1, which means that the situation is totally described under the Reuss limit, then equation (3.29) is simplified to equation (3.21) and consequently equation (3.28) is simplified to equation (3.20); if α equals 0, which means that the situation is totally described under the Voigt limit, then equation (3.29) is simplified to equation (3.26) and equation (3.28) is simplified to equation (3.25).

It has been argued that no situation can be totally described under the Voigt limit [8]. The minimum value of α is 0.5, which means these two models each contribute half to the total strains. This occurs when the uniaxial stress component t is very small. A large value of t causes the yielding of the crystallites, and therefore results in the isostress condition (α=1).

So far, no specific characteristics regarding the experimental setup of the powder X-ray diffraction techniques has been included. Whether the EDXD or ADXD technique is used, one is able to determine the strains under nonhydrostatic compression, as well as the stress state experienced by the sample. As indicated by equation (3.20), ψ, the angle between the load axis and the diffracting plane normal, is a very important parameter to be determined experimentally. The way one determines ψ is very different for the EDXD and the ADXD methods, as it will be shown in Chapter 4.

In the following Chapter, the two different methods used to extract the single crystal elastic constants, namely, the EDXD and the ADXD methods, will be presented. However, we will emphasize the ADXD method. So far, the details regarding the ADXD method reported in this work have not been found in any other publication. Thus we believe our approach is original.

Chapter 4. Determination of Single Crystal Elastic Constants Using Powder X-ray Diffraction

In this Chapter, details on how to use the EDXD and the ADXD method to determine the SCEC of a material are described, along with the derivation of some important equations, following the lattice strain theories discussed in Chapter 5.

4.1 The Energy Dispersive X-ray Diffraction (EDXD) Method

4.1.1 The Determination of Angle ψ

For the energy dispersive X-ray diffraction method, the wavelength of the incident X-ray beam is continuous over a broad range, and the diffraction angle 2θ is fixed by placing a collimator in front of the detector.

As shown in Figure 4.1, the angle of the diffracted X-ray beam makes with respect to the incident X-ray beam is 2θ, namely, the diffraction angle or the Bragg angle. As the wavelength of the incident X-ray beam is continuous, according to the Bragg's law, only those lattice planes {hkl} bisecting the diffraction angle 2θ contribute to the diffraction recorded at the detector, whatever the Miller indices they may have. [hkl] is the plane normal of these diffracting planes, which apparently bisects the angle π-2θ (the angle that the diffracted x-ray beam makes with respect to the incident X-ray beam in the other

way). All of the incident X-ray beam, the diffracted X-ray beam, and the diffracting plane normal [hkl] are in the same plane (plane A in Figure 4.1).

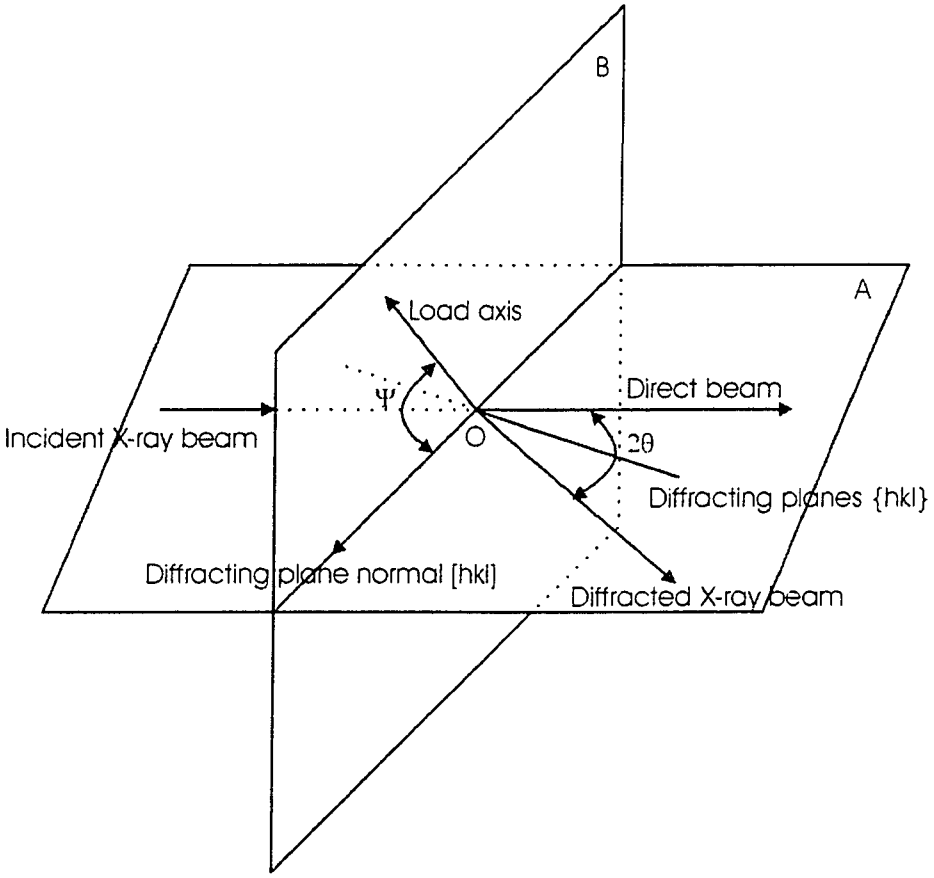

Figure 4.1 Coordinate system for the EDXD method. Plane A: incident X-ray beam, diffracted X-ray beam, and diffracting plane normal. Plane B: load axis and diffracting plane normal.

For the energy dispersive X-ray diffraction, once the relative position of the detector with respect to the incident beam is set, the selection of the lattice planes that contribute to the diffraction at the point of observation is established. Among all the lattice planes of

all the crystallites inside the DAC, only those lattice planes with their plane normals orientated along [hkl], as shown in Figure 4.1, have been selected.

Also shown in Figure 4.1, plane B is perpendicular to plane A, and these two planes intercept along the diffracting plane normal [hkl]. With a proper experimental setup, one can have the load axis aligned in plane B as shown in the Figure 4.1, and make an angle ψ with respect to the diffracting plane normal [hkl]. One rotates the DAC in plane B as to vary the angle ψ over a range from 0 to 90°.

Therefore, for the energy dispersive X-ray diffraction method, the angle ψ is adjusted and determined experimentally. Then using equation (3.20), the information on the single crystal elastic constants can be extracted. This is the fundamental aspect of the energy dispersive X-ray diffraction method.

4.1.2 The Estimation of the Uniaxial Stress Component (USC)

The determination of the single crystal elastic constants requires the knowledge of the uniaxial stress component t. In practice, t is estimated from the recorded X-ray diffraction patterns.

Under one specific load, the magnitude of the created shear stress t has one corresponding value. As discussed above, from the experimental setup we are able to determine ψ, the angle between the load axes with respect to the plane normals of all the selected diffracting planes. Changing systematically the angle ψ, a set of corresponding d-spacings can be determined.

For a specific diffraction condition with Miller indices hkl, substituting the set of ψ's and the corresponding d-spacings into equation (3.20), the corresponding values of Q(hkl) can be determined. Consequently, the corresponding values of Q(hkl) for all the observed X-ray diffraction lines can be determined as well.

For the cubic system under both the Reuss and Voigt limits, the uniaxial stress component t can then be estimated by [8]

$$t = 6G\langle Q(hkl)\rangle f(x,\alpha), \tag{4.1.1}$$

where

$$f(x,\alpha) = f_1 / f_2, \tag{4.1.2}$$

$$f_1 = \frac{2x+3}{10} + \frac{5x}{2(3x+2)}, \tag{4.1.3}$$

$$f_2 = \alpha[x - 3(x-1)\langle \Gamma(hkl)\rangle] + \frac{5x(1-\alpha)}{3x+2}, \tag{4.1.4}$$

and

$$x = 2(S_{11} - S_{12}) / S_{44}. \tag{4.1.5}$$

$\langle Q(hkl)\rangle$ and $\langle \Gamma(hkl)\rangle$ represent the corresponding averaged value over all the observed reflections. G is the shear modulus, which must be estimated by other measurements, such as the ultrasonic method [8]. $f(x,\alpha)$ is the factor taking into account the anisotropy and parameter α is defined in section 3.4, Chapter 3.

As a first approximation, the factor $f(x,\alpha)$ is ignored and the uniaxial stress component t is estimated by

$$t = 6G\langle Q(hkl)\rangle, \tag{4.1.6}$$

as t has been shown to depend only weakly on anisotropy [9, 12, 13]. Note that equation (4.1.6) is strictly true only for elastically isotropic materials.

4.1.3 Application of the EDXD Method

In this Section, a special case, namely, the cubic system under the Reuss limit, is taken as an example to determine the SCEC using the EDXD method.

First, angle ψ is systematically changed during the course of an experiment, and a set of corresponding diffraction patterns are recorded. Then using equation (3.20), the corresponding values of Q(hkl) are determined for all the observed diffraction lines. Note that in equation (3.20), d_{hkl}^{P}, the d-spacing corresponding to the situation under hydrostatic pressure, is obtained by setting ψ at an approximate angle of 54.7° (i.e., for the case where $1-3\cos^2\psi = 0$).

First, all the values of Q(hkl) are used to estimate the uniaxial stress component t, as discussed in the previous section, and then are used to determine the single crystal elastic compliances of a material.

Equation (3.21) is rewritten as [9, 12, 13]

$$Q(hkl) = m_0 + m_1\Gamma(hkl), \tag{4.1.7}$$

where

$$m_0 = \frac{t}{3}(S_{11} - S_{12}) \tag{4.1.8}$$

and

$$m_1 = -t\,(S_{11} - S_{12} - S_{44}/2)\,. \qquad (4.1.9)$$

By substituting all values of Q(hkl) and the corresponding Γ(hkl) into equation (4.1.7), one is able to determine the values of S_{11}-S_{12} and $(S_{11}$-S_{12}-$S_{44})/2$.

In order to determine all these three elastic compliances, namely, S_{11}, S_{12}, and S_{44}, one needs three independent equations. Using the knowledge of the equation of state under hydrostatic pressure for the concerned material, a third equation can be obtained from the isothermal bulk modulus K, where [9, 12, 13]

$$K^{-1} = 3\,(S_{11} + 2S_{12})\,. \qquad (4.1.10)$$

For the cubic system under the Reuss limit, the equation of state under hydrostatic pressure provides one independent equation, the elastic strains under nonhydrostatic compression provide the additional two independent equations, needed to determine the three single-crystal compliances. This is the reason for which all these measurements must be carried out under nonhydrostatic compression, as mentioned before.

4.2 The Angle Dispersive X-ray Diffraction (ADXD) Method

4.2.1. Defining ψ as a Function of the Azimuthal Angle ϕ and the Diffraction Angle 2θ

The incident X-ray beam is monochromatic for the angle dispersive X-ray diffraction technique and the detector is a two-dimensional X-ray recording image plate (details were given in Chapter 2). In this case, as the angle ψ depends on both the azimuthal angle

ϕ and the diffraction angle 2θ (details are given in the following; referring to Figure 4.2), it cannot be determined directly from the experimental setup as done for the energy dispersive X-ray diffraction method.

For the energy dispersive X-ray diffraction method, all the selected diffracting planes have their plane normals orientated along the same direction, whatever Miller indices they might correspond to. Therefore, the angle ψ is the same for all the diffracting planes.

For the angle dispersive X-ray diffraction method, the diffracting plane normals with different Miller indices are along different directions. Moreover, the diffracting plane normals corresponding to different points on the same Debye ring (with the same Miller index) are along different directions as well. In this case, the determination of the angle ψ involves the measurements of both the azimuthal angle ϕ and the diffraction angle 2θ.

We first consider the parallel geometry, where the direction of the incident X-ray beam coincides with the load axis (see also Figure 2.1). For powder X-ray diffraction, the diffracting plane normals with the same Miller indices form a cone placed symmetrically around the incident X-ray beam, and hence symmetrically about the loading axis as well. The angle ψ is thus the same for all the diffracting plane normals with the same Miller indices. Therefore, the effect of the uniaxial stress component t on all the diffracting planes with the same Miller indices is identical. Consequently, the Debye rings recorded on the image plate are perfect circles (assuming the incident X-ray beam is perpendicular to the plane of the detector).

In the case of the perpendicular geometry (Figure 2.1), where the direction of the load axis is perpendicular to the incident X-ray beam, the diffracting plane normals with the same Miller indices no longer form a uniform cone around the direction of the incident

X-ray beam, due to the influence of the uniaxial stress t (details are discussed in section 4.2.2). Depending on the azimuthal angle ϕ and the diffraction angle 2θ, the angle ψ is different from point to point on the Debye rings. The determination of angle ψ in terms of the azimuthal angle ϕ and the diffraction angle 2θ is as follows.

As shown in Figure 4.2, plane A contains both the load axis and the incident X-ray beam, and the incident x-ray beam makes an angle γ with respect to the load axis. A (X, Y, Z) coordinate system is defined, where the origin O is located at the sample, i.e., where X-ray diffraction occurs, the Z-axis points to the opposite direction of incident X-ray beam, the X-axis is perpendicular to the Z-axis and lies in plane A, and Y-axis is perpendicular to plane A so that an orthogonal right-handed coordinate system is defined.

Plane B contains both the incident X-ray beam and an arbitrary diffracting plane normal [hkl] satisfying Bragg's law. The diffracted X-ray beam OP lies in plane B as well, as the incident X-ray beam, the diffracting plane normal [hkl], and the diffracted X-ray beam are in the same plane.

The angle between the diffracted X-ray beam and the incident X-ray beam (Z-axis) is the Bragg diffraction angle 2θ. The angle between the diffracting plan normal [hkl] and Z-axis is $\pi/2-\theta$. The angle between the diffracting plane normal [hkl] and the load axis is Ψ. The angle between plane A and plane B is ϕ, namely, the azimuthal angle. Both angles Ψ and 2θ are dependent on the azimuthal angle ϕ, due to the influence of the uniaxial stress (along the load axis).

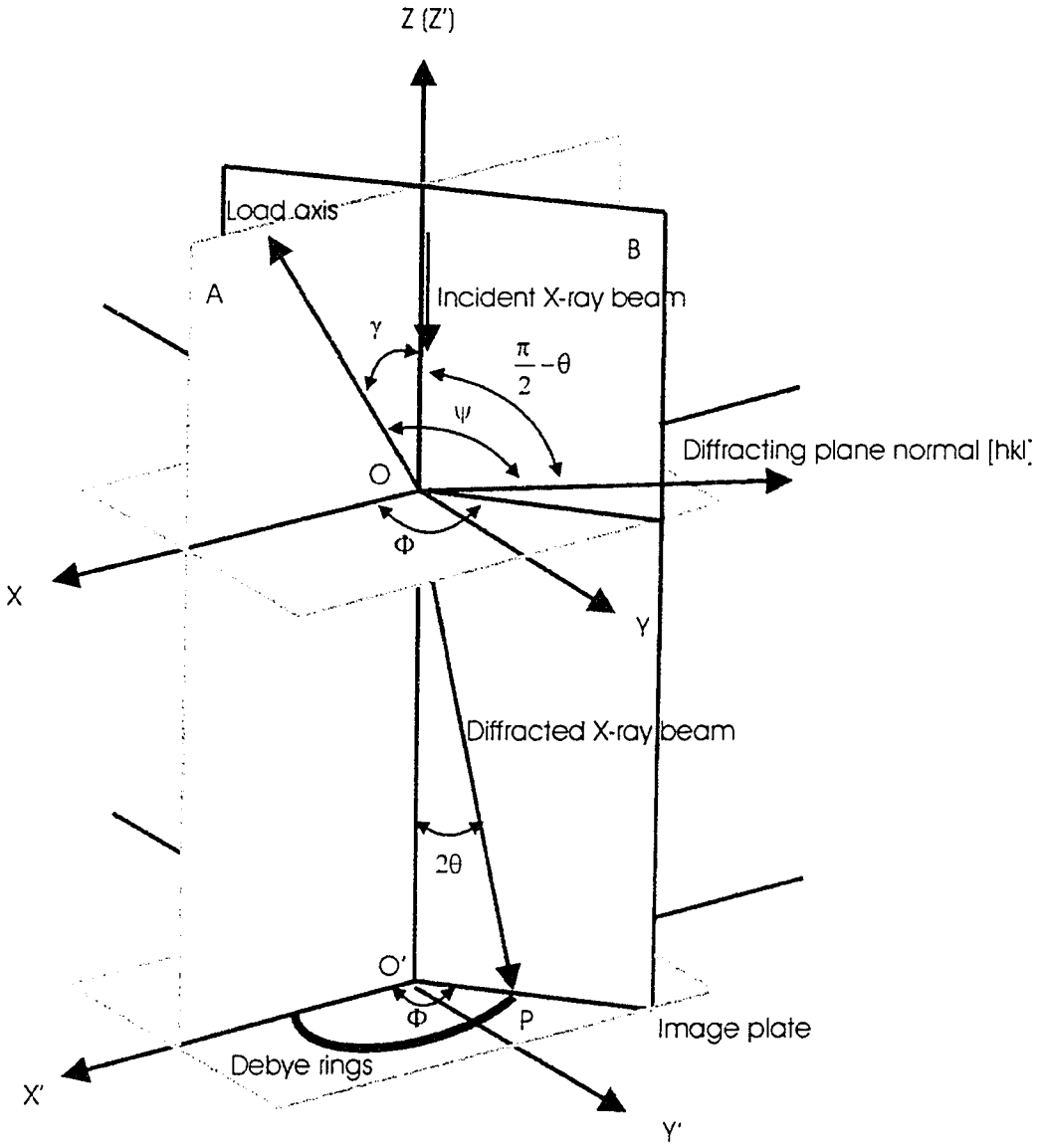

Figure 4.2 Coordinate systems for ADXD. Plane A: incident X-ray beam, load axis. Plane B: incident and diffracted X-ray beam, diffracting plane normal.

Another coordinate system, namely, the (X', Y', Z') coordinate system needs to be defined. As shown in Figure 4.2, Z'-axis coincides with the Z-axis; X'-axis and Y'-axis

are parallel to the X-axis and Y-axis, respectively. In reality, the X'Y' plane represents the plane of the two-dimensional X-ray recording image plate, which is usually placed perpendicularly to the incident X-ray beam. O' is the point where the undiffracted X-ray beam hits the image plate. P is the point where the diffracted X-ray beam hits the image plate, corresponding to one point on a Debye ring recorded on the image plate. O'P is the intersection of plane B and the image plate (X'Y' plane), which is used to determine the diffraction angle 2θ. The angle between O'P and X'-axis is the azimuthal angle ϕ.

In the (X, Y, Z) coordinate systems defined above, the load axis (parallel to σ_3) is represented by the unit vector $\sin\gamma\,\bar{i}+\cos\gamma\,\bar{k}$; the diffracting plane normal [hkl] is represented by the unit vector $\cos\theta\cos\phi\,\bar{i}+\cos\theta\sin\phi\,\bar{j}+\sin\theta\,\bar{k}$. Then the cosines of Ψ, the angle between the diffracting plane normal [hkl] and load axis, is the dot product of these two vectors:

$$\cos\psi=\sin\gamma\cos\phi\cos\theta+\cos\gamma\sin\theta\ . \tag{4.2.1}$$

Equation (4.2.1) is in agreement with that of reference [14].

For any point on a Debye ring recorded on the image plate (X'Y' plane), both the azimuthal angle ϕ and the diffraction angle 2θ (related to O'P) can be read directly using, for instance, SimPa [26]. The angle γ can be determined from the experimental setup. Therefore, using equation (4.2.1), the corresponding angle ψ of any point on a Debye ring can be determined.

As both ψ and 2θ are dependent on the azimuthal angle ϕ and the Miller indices hkl, equation (4.2.1) is rewritten as

$$\cos\psi_{hkl}(\phi)=\sin\gamma\cos\phi\cos\theta_{hkl}(\phi)+\cos\gamma\sin\theta_{hkl}(\phi)\ , \tag{4.2.2}$$

where the subscript *hkl* indicates the corresponding value is dependent on the Miller indices.

4.2.2. A Different Approach: The ADXD Method

For the method using ADXD to measure the SCEC, substituting equation (4.2.2) into equation (3.20), one obtains

$$d_{hkl}^{p+d}(\phi) = d_{hkl}^{p}\{1+[1-3\cos^2\psi_{hkl}(\phi)]Q(hkl)\}. \tag{4.2.3}$$

As defined before, the superscript $p+d$ stands for "under nonhydrostatic pressure", p stands for "under the corresponding hydrostatic pressure only". Note that for the angle dispersive X-ray diffraction method, the d-spacings depend on the azimuthal angle ϕ as well. Equation (4.2.3) can be rewritten as

$$d_{hkl}^{p+d}(\phi) = d_{hkl}^{p} + \Delta d_{hkl}^{d}(\phi), \tag{4.2.4}$$

where

$$d_{hkl}^{p} = d_{hkl}^{0}(1+\varepsilon^{p}) = d_{hkl}^{0}[1+(S_{11}+2S_{12})\sigma_{p}], \tag{4.2.5}$$

and

$$\Delta d_{hkl}^{d}(\phi) = d_{hkl}^{p}\left(\frac{t}{3}\right)[1-3\cos^2\psi_{hkl}(\phi)](S_{11}-S_{12}-3S\Gamma). \tag{4.2.6}$$

d_{hkl}^{p}, the d-spacing of lattice plane (hkl) under hydrostatic pressure, is independent of the azimuthal angle ϕ, as the Debye rings under the hydrostatic compression are perfect circles. $\Delta d_{hkl}^{d}(\phi)$ is the "d-spacing" introduced by the deviatoric stress only and it depends on the azimuthal angle ϕ.

Substituting equations (4.2.5) and (4.2.6) into equation (4.2.4), one obtains

$$d_{hkl}^{p+d}(\phi) = d_{hkl}^{0}[1+(S_{11}+2S_{12})\sigma_p] + d_{hkl}^{p}\left(\frac{t}{3}\right)[1-3\cos^2\psi_{hkl}(\phi)](S_{11}-S_{12}-3S\Gamma). \quad (4.2.7)$$

Substituting (4.2.2) into (4.2.7), one has

$$\begin{aligned} d_{hkl}^{p+d}(\phi) &= d_{hkl}^{0}[1+(S_{11}+2S_{12})\sigma_p] \\ &+ d_{hkl}^{p}\left(\frac{t}{3}\right)\{1-3[\sin\gamma\cos\phi\cos\theta_{hkl}(\phi)+\cos\gamma\sin\theta_{hkl}(\phi)]^2\}(S_{11}-S_{12}-3S\Gamma). \end{aligned} \quad (4.2.8)$$

Equation (4.2.8) is the most general expression of the d-spacings for the angle dispersive X-ray diffraction method. As γ can always be determined from the experimental setup, equation (4.2.8) will be simplified significantly in practice.

If the incident X-ray beam is parallel to the loading axis, in other words, γ is set at 0° in Figure 4.2 (the DAC in the parallel geometry), equation (4.2.8) becomes

$$d_{hkl}^{p+d} = d_{hkl}^{0}[1+(S_{11}+2S_{12})\sigma_p] + d_{hkl}^{p}\left(\frac{t}{3}\right)(1-3\sin^2\theta_{hkl})(S_{11}-S_{12}-3S\Gamma). \quad (4.2.9)$$

It can be seen from equation (4.2.9) that θ_{hkl} is independent of the azimuthal angle ϕ for this special case, which indicates that the Debye rings recorded on the image plate should be perfect circles. This is in agreement with the analysis in the previous section and the practical observations [20, 21].

In Figure 4.2, if the incident X-ray beam is perpendicular to the load axis, i.e., γ is set at 90° (the DAC in the perpendicular geometry), equation (4.2.8) becomes

$$\begin{aligned} d_{hkl}^{p+d}(\phi) &= d_{hkl}^{0}[1+(S_{11}+2S_{12})\sigma_p] \\ &+ d_{hkl}^{p}\left(\frac{t}{3}\right)[1-3\cos^2\phi\cos^2\theta_{hkl}(\phi)](S_{11}-S_{12}-3S\Gamma). \end{aligned} \quad (4.2.10)$$

In this case, $\theta_{hkl}(\phi)$ is clearly dependent on the azimuthal angle ϕ.

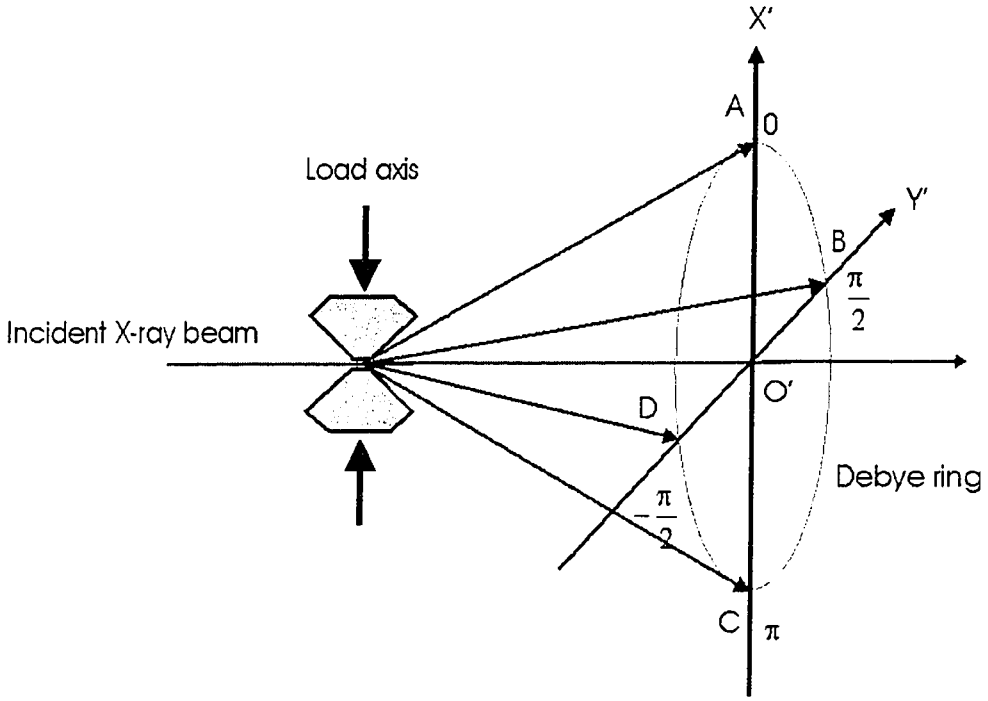

Figure 4.3 Four special points on a Debye ring. The azimuthal angles at points A, B, C and D are 0, $\pi/2$, π and $-\pi/2$, respectively.

As shown in Figure 4.3, four special points A, B, C and D on a given Debye ring are considered, for which the azimuthal angle ϕ equals 0, $\pi/2$, π, and $-\pi/2$, respectively. Substituting the four specific values of ϕ into equation (4.2.10), the following two equations are obtained for points A and C, and B and D, respectively:

$$d_{hkl}^{p+d}(0,\pi) = d_{hkl}^{0}[1+(S_{11}+2S_{12})\sigma_p] + d_{hkl}^{p}\left(\frac{t}{3}\right)[1-3\cos^2\theta_{hkl}(0,\pi)](S_{11}-S_{12}-3S\Gamma), \tag{4.2.11}$$

$$d_{hkl}^{p+d}(\pm\frac{\pi}{2}) = d_{hkl}^{0}[1+(S_{11}+2S_{12})\sigma_p] + d_{hkl}^{p}\left(\frac{t}{3}\right)(S_{11}-S_{12}-3S\Gamma). \tag{4.2.12}$$

Equations (4.2.11) and (4.2.12) can be rewritten as

$$d_{hkl}^{p+d}(0,\pi) = d_{hkl}^{p} + [1-3\cos^2\theta_{hkl}(0,\pi)]\,\Delta d_{hkl}^{d}(\pm\frac{\pi}{2}), \tag{4.2.13}$$

and

$$d_{hkl}^{p+d}(\pm\frac{\pi}{2}) = d_{hkl}^{p} + \Delta d_{hkl}^{d}(\pm\frac{\pi}{2}), \tag{4.2.14}$$

respectively, where d^{p}_{hkl} is given by (4.2.5) and

$$\Delta d_{hkl}^{d}(\pm\frac{\pi}{2}) = d_{hkl}^{p}\left(\frac{t}{3}\right)(S_{11} - S_{12} - 3S\Gamma). \tag{4.2.15}$$

Actually, points A and C (ϕ = 0 and π, respectively) correspond to the minimum d-spacings on a distorted Debye ring, whereas points B and D (ϕ = $\pm$ π/2, respectively) correspond to the maximum d-spacing.

As the corresponding diffraction angle 2θ at different azimuthal angle ϕ (ϕ = 0, π, and $\pm$ π/2) can be read directly from the X-ray recording image plate, therefore, using equations (4.2.13) and (4.2.14), both d_{hkl}^{p} and $\Delta d_{hkl}^{d}(\pm\frac{\pi}{2})$ can be calculated.

Once d_{hkl}^{p}, the d-spacing under purely hydrostatic pressure, is known, the corresponding hydrostatic pressure can be obtained from the equation of state. Using equation (4.2.5), the value of $S_{11}+2S_{12}$ can be determined. Here the equation of state under hydrostatic pressure provides one of the three independent equations, required to determine the three single crystal elastic compliances S_{11}, S_{12}, and S_{44}.

$\Delta d_{hkl}^{d}(\pm\frac{\pi}{2})$, the d-spacing at ϕ = $\pm$ π/2 due to the nonhydrostatic compression only, will provide another two of the three equations. Note that so far only one Debye ring has

been used. When two additional Debye rings with Γ different are used, three equations are obtained as follows:

$$\Delta d_1^d(\pm\frac{\pi}{2}) = d_1^p\left(\frac{t}{3}\right)(S_{11} - S_{12} - 3S\Gamma_1), \tag{4.2.16a}$$

$$\Delta d_2^d(\pm\frac{\pi}{2}) = d_2^p\left(\frac{t}{3}\right)(S_{11} - S_{12} - 3S\Gamma_2), \tag{4.2.16b}$$

$$\Delta d_3^d(\pm\frac{\pi}{2}) = d_3^p\left(\frac{t}{3}\right)(S_{11} - S_{12} - 3S\Gamma_3), \tag{4.2.16c}$$

where the subscripts 1, 2 and 3 indicate the different Miller indices. Γ_1, Γ_2, and Γ_3 are calculated from equation (3.17). The uniaxial stress component t is determined from equation (4.1.1) or (4.1.6), as discussed in section 4.1.2.

From equations (4.2.16a), (4.2.16b) and (4.2.16c), the values of $S_{11} - S_{12}$ and S can be obtained. As we have already obtained the value of $S_{11}+2S_{12}$ from equation (4.2.5), thus all the three single crystal elastic compliances can be calculated. Note that so far only four special points on each Debye ring and only three Debye rings (with Γ different) have been used. All the other points on each Debye ring and all the other Debye rings can be used to improve the accuracy.

4.2.3 Setting γ between 0 and 90°

As shown in Figure 2.1 (as well as shown in Figure 4.2), when γ is set at 0° (the DAC in the parallel geometry), the incident X-ray beams pass through the upper diamond, hit

the samples, then pass through the lower diamond. In this case, the X-ray beams do not interfere with the gasket, therefore the gasket needs not to be X-ray transparent.

When γ is set at 90° (the DAC in the perpendicular geometry, as shown in Figure 2.1), both the incident and the diffracted X-ray beams pass through the gasket. In this case, the gasket must be X-ray transparent; otherwise, the gasket will absorb the X-ray beams and no X-ray diffraction pattern can be recorded.

As shown in Figure 2.1, γ_m is the maximum angle for the DAC to pass the incident X-ray beam through the upper diamond, and the diffracted X-ray beam through the lower diamond without interfering with the gasket. If γ is set at an angle between 0 and γ_m (usually as close as possible to γ_m), it is possible to extract the information on the single crystal elastic constants without using the X-ray transparent gasket. It is worth noting that Dubrovinsky and co-workers [14] have successfully measured the elastic compliances for CsI and NaCl at $\gamma = 30^{\circ}$ without using an X-ray transparent gasket.

When γ is set at an arbitrary angle between 0 and 90°, take $\gamma = 45°$ for an example, equation (4.2.8) becomes

$$d_{hkl}^{p+d}(\phi) = d_{hkl}^{0}[1 + (S_{11} + 2S_{12})\sigma_p] + d_{hkl}^{p}\left(\frac{t}{3}\right)\{1 - \frac{3}{2}[\cos\phi\cos\theta_{hkl}(\phi) + \sin\theta_{hkl}(\phi)]^2\}(S_{11} - S_{12} - 3S\Gamma). \quad (4.2.17)$$

Following the method discussed in section 4.2.2, considering the four specific points at $\phi = 0$, π and $\pm\pi/2$, respectively, the following equations are obtained:

$$d_{hkl}^{p+d}(0) = d_{hkl}^{0}[1 + (S_{11} + 2S_{12})\sigma_p] + d_{hkl}^{p}\left(\frac{t}{3}\right)\{1 - \frac{3}{2}[\cos\theta_{hkl}(0) + \sin\theta_{hkl}(0)]^2\}(S_{11} - S_{12} - 3S\Gamma), \quad (4.2.18)$$

$$d_{hkl}^{p+d}(\pi) = d_{hkl}^{0}[1 + (S_{11} + 2S_{12})\sigma_p] + d_{hkl}^{p}\left(\frac{t}{3}\right)\{1 - \frac{3}{2}[\cos\theta_{hkl}(\pi) - \sin\theta_{hkl}(\pi)]^2\}(S_{11} - S_{12} - 3S\Gamma) \quad (4.2.19)$$

and

$$d_{hkl}^{p+d}(\pm\frac{\pi}{2}) = d_{hkl}^{0}[1 + (S_{11} + 2S_{12})\sigma_p] + d_{hkl}^{p}\left(\frac{t}{3}\right)[1 - \frac{3}{2}\sin^2\theta_{hkl}(\pm\frac{\pi}{2})](S_{11} - S_{12} - 3S\Gamma). \quad (4.2.20)$$

Note that in this case the d-spacings at 0 and π are different, which is unlike the situation encountered where γ equals 90°. Reading the corresponding 2θ at ϕ = 0, π, and ± π/2, respectively, considering three Debye rings with different geometry factor Γ as described in Section 4.2.2, the three single crystal elastic compliances can be determined. In principle, no matter at which value the angle γ is set (except for 0°), the single crystal elastic constants can be determined.

However, the symmetry of the Debye rings recorded on the image plate is dependent on γ, the angle between the incident x-ray beam and the load axis. As γ equals 0°, all the Debye rings are perfect circles as described by equation (4.2.9); as γ equals to 90°, all the Debye rings are elongated along the X'-axis and compressed along the Y'-axis (in terms of 2θ), due to the applied deviatoric stress. Therefore, the Debye rings are no longer

perfect circles. However, the Debye rings are symmetric with respect to both the X′-axis and Y′-axis, as described by equations (4.2.11) and (4.2.12).

Setting γ at an arbitrary angle between 0 and 90°, such as 45°, the Debye rings are symmetric about the X′-axis, but are no longer symmetric with respect to the Y′-axis.

4.2.4 Application of the ADXD Method

As described in Section 4.2.2, under a specific load, one is able to determine the corresponding hydrostatic pressure P, the unaxial stress component t, and the single crystal elastic compliances S_{11}, S_{12}, and S_{44} of a cubic system from the recorded X-ray diffraction image. Changing the load systematically on the sample, a set of data, as listed in Table 4.1, can be obtained.

Table 4.1 Experimental data under different loads.

Load	Hydrostatic pressure P	Uniaxial stress component t	Single crystal elastic compliance S_{ij}		
1	P_1	$t_1(P_1)$	$S_{11}(P_1)$	$S_{12}(P_1)$	$S_{44}(P_1)$
2	P_2	$t_2(P_2)$	$S_{11}(P_2)$	$S_{12}(P_2)$	$S_{44}(P_2)$
3	P_3	$t_3(P_3)$	$S_{11}(P_3)$	$S_{12}(P_3)$	$S_{44}(P_3)$
	.....	.....	.....	.....	.....
n	P_n	$t_n(P_n)$	$S_{11}(P_n)$	$S_{12}(P_n)$	$S_{44}(P_n)$

From Table 4.1, a relationship between the induced unaxial stress component t and the corresponding hydrostatic pressure P can be estimated [12, 13]:

$$t = t_0 + xP. \tag{4.2.21}$$

The relationships between the single crystal elastic compliance and the stiffness are as follows [1]:

$$C_{11} = \frac{S_{11} + S_{12}}{(S_{11} - S_{12})(S_{11} + 2S_{12})}, \tag{4.2.22}$$

$$C_{12} = \frac{-S_{12}}{(S_{11} - S_{12})(S_{11} + 2S_{12})}, \tag{4.2.23}$$

$$C_{44} = \frac{1}{S_{44}}. \tag{4.2.24}$$

Using equations (4.2.22), (4.2.23) and (4.2.24), one is able to determine the corresponding single crystal elastic stiffness, as well as the pressure derivatives of second-order elastic moduli $\frac{\partial C_{11}}{\partial \mathrm{P}}$, $\frac{\partial C_{12}}{\partial \mathrm{P}}$, and $\frac{\partial C_{44}}{\partial \mathrm{P}}$. The corresponding single crystal elastic stiffness under an arbitrary pressure can then be estimated using the equations

$$C_{11} = C_{11}^0 + P\left(\frac{\partial C_{11}}{\partial P}\right), \tag{4.2.25a}$$

$$C_{12} = C_{12}^0 + P\left(\frac{\partial C_{12}}{\partial P}\right), \tag{4.2.25b}$$

and

$$C_{44} = C_{44}^0 + P\left(\frac{\partial C_{44}}{\partial P}\right), \tag{4.2.25c}$$

where, C_{ij}^{0} denotes the corresponding single crystal elastic stiffness under the ambient pressure.

The method described in Section 4.1.3 for the energy dispersive X-ray diffraction can be used for the angle dispersive X-ray diffraction as well. However, the ADXD method combined with a two dimensional X-ray recording image plate provides much convenience in practical applications.

For angle dispersive X-ray diffraction combined with a two-dimensional X-ray recording image plate, complete Debye rings can be recorded. As γ is usually set at 90^{o} (DAC in the perpendicular geometry), equation (4.2.2) becomes

$$\cos\psi_{hkl}(\phi) = \cos\phi\cos\theta_{hkl}(\phi). \tag{4.2.23}$$

For one specific Debye ring recorded on the X-ray diffraction image, as the azimuthal angle ϕ changes from 0 to 90^{o}, ψ changes from θ_{hkl} to 90^{o}. Therefore, for the Debye rings recorded on the image plate, one has all the points corresponding to different situations, for which ψ changes from θ_{hkl} to 90°. It is worth emphasizing that all the information is obtained on a single X-ray diffraction image.

In comparison, for the energy dispersive X-ray diffraction method, one has to set ψ at different values each time and record all the corresponding X-ray diffraction patterns. As one value of ψ provides one data point, ψ must be changed as many times as necessary, to obtain enough data, in order to achieve an acceptable accuracy. While for the angle dispersive X-ray diffraction, infinite number of data points can be recorded on a single X-ray diffraction image.

For the energy dispersive X-ray diffraction method, ψ must be set at 54.7°, in order to estimate the corresponding hydrostatic pressure [12, 13]. While for the angle dispersive X-ray diffraction, as discussed in section 4.2.2, reading from the image the diffraction angle 2θ at two specific points on any Debye ring (one at $\phi = 0°$ and the other at $\phi = 90°$), using equations (4.2.13) and (4.2.14), the corresponding hydrostatic pressure can be determined.

We believe the ADXD method provide more advantages than the EDXD method in real applications.

Chapter 5. Results and Discussion

In this Chapter, we summarize the experimental attempts at measuring SCEC under nonhydrostatic compression, and carry out theoretical calculations about the d-spacings of Mo under different pressure and at different points on Debye rings, using the important equations we have derived for the ADXD method.

5.1 Experimental Attempts at Measuring SCEC Under Compression

Attempts to determine the SCEC of molybdenum were made using the ADXD method using the synchrotron radiation available at the B2-line of the Cornell High Energy Synchrotron Source (CHESS). As described in Chapter 2, the measurement was carried out using the perpendicular geometry. A powder sample of molybdenum was placed in the high pressure chamber of a DAC without using any pressure transmitting medium, in order to generate a nonhydrostatic pressure condition. The gasket was made out of Be, which is transparent to hard X-rays.

However, our attempts did not achieve the expected goals. Figure 5.1 shows the X-ray diffraction image of Mo recorded under nonhydrostatic pressure, for which the corresponding hydrostatic pressure is 1.3 GPa. It seemed that the Be gasket was not strong enough to hold the sample inside the high pressure chamber, and therefore failed to generate the necessary high pressure conditions. An analysis of the recorded X-ray

diffraction patterns indicated that the pressure inside the DAC had never gone beyond 2 GPa. Observation under the microscope indicated that the Be gasket had flowed to a large extent under the load.

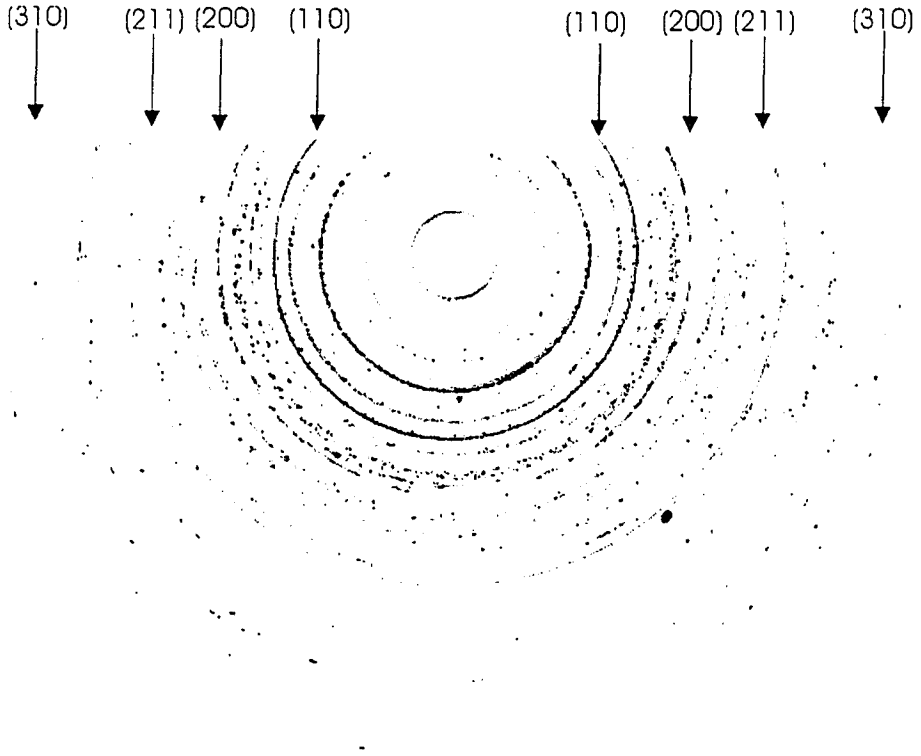

Figure 5.1 Image of X-ray diffraction patterns of Mo recorded under nonhydrostatic compression, for which the corresponding hydrostatic pressure is 1.3 GPa. X-ray diffraction lines (110), (200), (211) and (310) were indicated on the image. The tiny dots might come from the Be gasket. Other unidentified rings correspond to X-ray diffraction arising from the X-ray beam collimator and stop.

As the Be gasket was not strong enough, the sample was pushed aside as the diamond anvils moved towards each other. For the perpendicular geometry, the X-ray beam is

perpendicular to the load axis, and passes through the gasket. Therefore, the sample became fairly thick in the direction along the incident X-ray beam, and hence the recorded X-ray diffraction pattern on an image plate was broad. Moreover, the background due to the Be gasket interfered with the X-ray diffraction pattern, making it difficult to recognize the clear boundary of a Debye ring as illustrated in Figure 5.1.

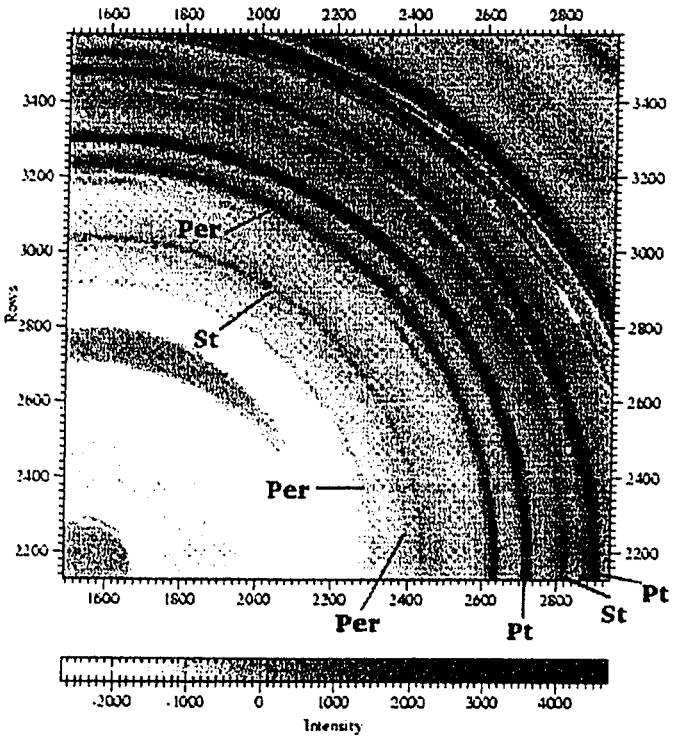

Figure 5.2 X-ray diffraction pattern for perovskite experiment at P = 25 GPa. Debye rings from perovskite, stishovite, and platinum are shown. Background from amorphous boron was substracted for this pattern. Reproduced from [30].

Despite the failure of our attempts, we still emphasize the feasibility of the ADXD method. Using X-ray transparent gaskets made of beryllium drilled and filled with amorphous boron, the ADXD method has been successfully carried out up to 25 GPa, on several kinds of polycrystalline samples [30].

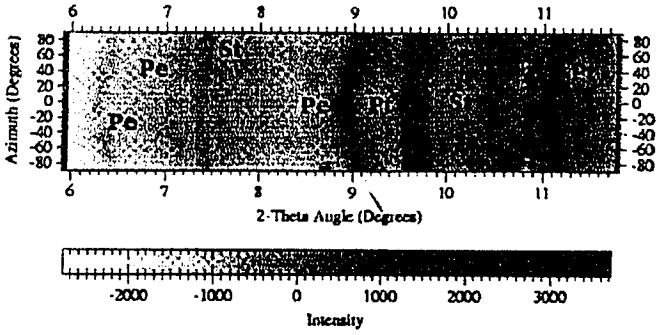

Figure 5.3 Image of X-ray diffraction patterns for perovskite and platinum experiment at P = 25 GPa. The X-ray diffraction angle 2θ is plotted as a function of the azimuthal angle ϕ (between –90 and 90°) in a Cartesian coordinate system. Reproduced from [30].

Figure 5.2 shows the X-ray diffraction pattern for sample of (Mg, Fe)SiO_3 perovskite. It can be seen clearly in Figure 5.3 (Note: The X-ray diffraction image has been "unrolled" as to display the data on a Cartesian plot) that the Debye rings are elongated mostly at the points where the azimuthal angle ϕ equals 0°, while compressed mostly at the points where the azimuthal angle equals ±90° (in terms of a 2θ profile). The practical observations are in agreement with the calculations and predictions carried out in Chapter 4.

If the X-ray diffraction patterns of molybdenum like those shown in Figure 5.3 for perovskite could be recorded, using the ADXD method discussed in Chapter 4, it should be able to determine the SCEC of molybdenum. In the following Section, we will calculate the effects of nonhydrostatic pressure conditions on molybdenum.

5.2 Impact of Nonhydrostatic Pressure on Debye Rings

In this Section, molybdenum is taken as an example to illustrate the change in d-spacing on Debye rings, due to nonhydrostatic pressure, as calculated by the equations obtained for the ADXD method as discussed in Chapter 4. All the data used for the calculation are taken from reference [13]. The uniaxial stress t is taken as

$$t = 0.46 + 0.13\,P \text{ (GPa)}, \tag{5.1}$$

following Duffy *et al.* [13]. The single crystal stiffness tensor elements C_{11}, C_{12}, and C_{44} under ambient pressure are read directly from Figure 10 in reference [13], and they are 470, 160, and 110 GPa, respectively. The pressure derivatives of second-order elastic moduli $\frac{\partial C_{11}}{\partial P}$, $\frac{\partial C_{11}}{\partial P}$ and $\frac{\partial C_{11}}{\partial P}$ are taken from Table 3 of reference [13], namely, 7.3, 3.3 and 0.5, respectively. Therefore the single crystal stiffness tensor elements $C_{11}(P)$, $C_{12}(P)$, and $C_{44}(P)$ under an arbitrary pressure P can be described as

$$C_{11}(P) = 470 + 7.3\,P, \tag{5.2}$$

$$C_{12}(P) = 160 + 3.3\,P, \tag{5.3}$$

and

$$C_{44}(P) = 110 + 0.5\,P, \tag{5.4}$$

respectively. Although there are uncertainties associated with the determination of single crystal elastic stiffness C_{ij} in Figure 10 in reference [13], we assume the data taken from the best fit line are accurate.

All the equations derived for the ADXD method in this work are based on single crystal elastic compliance elements S_{ij}. Single crystal elastic stiffness elements C_{ij} can be transformed into compliance elements S_{ij} as follows [1]:

$$S_{11} = \frac{C_{11} + C_{12}}{(C_{11} - C_{12})(C_{11} + 2C_{12})}, \tag{5.5}$$

$$S_{12} = \frac{-C_{12}}{(C_{11} - C_{12})(C_{11} + 2C_{12})}, \tag{5.6}$$

$$S_{44} = \frac{1}{C_{44}}. \tag{5.7}$$

Substituting equations (5.2) and (5.3) into equations (5.5) and (5.6), substituting equation (5.4) into equation (5.7), all the compliance S_{ij} under an arbitrary pressure, i.e., $S_{11}(P)$, $S_{12}(P)$, and $S_{44}(P)$ can be estimated.

Substituting $S_{11}(P)$, $S_{12}(P)$, and $S_{44}(P)$ into equations (4.2.5), (4.2.11) and (4.2.12), the d-spacings at points where the pressure conditions correspond to the hydrostatic one, where the azimuthal angle equals 0°, and where the azimuthal angle equals 90°, are determined, respectively. Tables 5.1, 5.2, 5.3, and 5.4 list the d-spacings and the corresponding 2θ, at the three points as indicated above on a Debye ring, under different pressures, for diffraction line (110), (200), (211), and (310), respectively. We have kept 4 decimal places for the calculated d-spacings in all these tables, although practically we can measure the d-spacings up to 3 decimal places only. The same comment applies also to Tables 5.5 to 5.8.

Figures 5.4, 5.5, 5.6 and 5.7 illustrate the change of the d-spacings at the three points under different pressures for the diffraction line (110), (200), (211), and (310), respectively. The difference in the d-spacings at the three points increases with the applied pressure, due to the fact that the uniaxial stress t increases linearly with the applied pressure (as indicated by equation (5.1)).

Table 5.1 Calculated d-spacings and 2θ for Mo at the points under the corresponding hydrostatic pressure, azimuthal angle equals 0° and 90°, respectively, for diffraction line (110) under different pressures. d_p (Å) and 2θ_p (°) stand for the d-spacing and X-ray diffraction angle 2θ under the corresponding hydrostatic pressure. d_90 (Å) and 2θ_90 (°) stand for the d-spacing and X-ray diffraction angle 2θ at the point where the azimuthal angle is ±90 degrees. d_0 (Å) and 2θ_0 (°) stand for the d-spacing and X-ray diffraction angle 2θ at the point where the azimuthal angle is 0 degree.

P (GPa)	d_p (Å)	2θ_p (°)	d_90 (Å)	2θ_90 (°)	d_0 (Å)	2θ_0 (°)
0	2.2251	12.7958	2.2262	12.7894	2.2229	12.8084
5	2.2122	12.8709	2.2147	12.8565	2.2073	12.8995
10	2.2012	12.9356	2.2049	12.9138	2.1939	12.9788
15	2.1917	12.9917	2.1965	12.9635	2.1824	13.0475
20	2.1835	13.0410	2.1892	13.0068	2.1722	13.1088
25	2.1762	13.0845	2.1828	13.0450	2.1633	13.1630
30	2.1698	13.1233	2.1772	13.0789	2.1555	13.2109
35	2.1641	13.1581	2.1721	13.1092	2.1483	13.2552
40	2.1590	13.1894	2.1677	13.1364	2.1420	13.2944
45	2.1544	13.2178	2.1636	13.1610	2.1363	13.3300
50	2.1502	13.2436	2.1599	13.1833	2.1310	13.3633

Table 5.2 Calculated d-spacings and 2θ for Mo at points under the corresponding hydrostatic pressure, azimuthal angle equals 0° and 90°, respectively, for diffraction (200) under different pressures. d_p (Å) and 2θ_p (°) stand for the d-spacing and X-ray diffraction angle 2θ under the corresponding hydrostatic pressure. d_90 (Å) and 2θ_90 (°) stand for the d-spacing and X-ray diffraction angle 2θ at the point where the azimuthal angle is ±90 degrees. d_0 (Å) and 2θ_0 (°) stand for the d-spacing and X-ray diffraction angle 2θ at the point where the azimuthal angle is 0 degree.

P (GPa)	d_p (Å)	2θ_p (°)	d_90 (Å)	2θ_90 (°)	d_0 (Å)	2θ_0 (°)
0	1.5734	18.1339	1.5742	18.1250	1.5719	18.1509
5	1.5643	18.2409	1.5660	18.2203	1.5609	18.2803
10	1.5565	18.3330	1.5591	18.3020	1.5514	18.3930
15	1.5498	18.4129	1.5531	18.3726	1.5433	18.4906
20	1.5439	18.4829	1.5480	18.4344	1.5362	18.5774
25	1.5388	18.5450	1.5435	18.4887	1.5299	18.6537
30	1.5343	18.6002	1.5395	18.5370	1.5243	18.7230
35	1.5303	18.6496	1.5359	18.5801	1.5193	18.7851
40	1.5266	18.6943	1.5328	18.6188	1.5149	18.8408
45	1.5234	18.7346	1.5299	18.6538	1.5108	18.8918
50	1.5204	18.7714	1.5273	18.6856	1.5071	18.9386

Table 5.3 Calculated d-spacings and 2θ for Mo at points under the corresponding hydrostatic pressure, azimuthal angle equals 0° and 90°, respectively, for diffraction (211) under different pressures. d_p (Å) and 2θ_p (°) stand for the d-spacing and X-ray diffraction angle 2θ under the corresponding hydrostatic pressure. d_90 (Å) and 2θ_90 (°) stand for the d-spacing and X-ray diffraction angle 2θ at the point where the azimuthal angle is ±90 degrees. d_0 (Å) and 2θ_0 (°) stand for the d-spacing and X-ray diffraction angle 2θ at the point where the azimuthal angle is 0 degree.

P (GPa)	d_p (Å)	2θ_p (°)	d_90 (Å)	2θ_90 (°)	d_0 (Å)	2θ_0 (°)
0	1.2847	22.2564	1.2853	22.2454	1.2835	22.2774
5	1.2772	22.3885	1.2786	22.3630	1.2745	22.4360
10	1.2709	22.5018	1.2730	22.4637	1.2669	22.5737
15	1.2654	22.6003	1.2681	22.5508	1.2602	22.6948
20	1.2606	22.6868	1.2639	22.6269	1.2544	22.8009
25	1.2564	22.7633	1.2602	22.6939	1.2493	22.8949
30	1.2528	22.8312	1.2570	22.7534	1.2448	22.9794
35	1.2495	22.8924	1.2541	22.8065	1.2407	23.0555
40	1.2465	22.9473	1.2515	22.8543	1.2371	23.1243
45	1.2438	22.9972	1.2492	22.8975	1.2338	23.1865
50	1.2414	23.0425	1.2471	22.9367	1.2308	23.2437

Table 5.4 Calculated d-spacings and 2θ for Mo the points under the corresponding hydrostatic pressure, azimuthal angle equals 0° and 90°, respectively, for diffraction (310) under different pressures. d_p (Å) and 2θ_p (°) stand for the d-spacing and X-ray diffraction angle 2θ under the corresponding hydrostatic pressure. d_90 (Å) and 2θ_90 (°) stand for the d-spacing and X-ray diffraction angle 2θ at the point where the azimuthal angle is ±90 degrees. d_0 (Å) and 2θ_0 (°) stand for the d-spacing and X-ray diffraction angle 2θ at the point where the azimuthal angle is 0 degree.

P (GPa)	d_p (Å)	2θ_p (°)	d_90 (Å)	2θ_90 (°)	d_0 (Å)	2θ_0 (°)
0	0.9951	28.8567	0.9956	28.8422	0.9942	28.8832
5	0.9893	29.0293	0.9904	28.9961	0.9873	29.0901
10	0.9844	29.1777	0.9860	29.1278	0.9814	29.2688
15	0.9802	29.3066	0.9823	29.2417	0.9763	29.4247
20	0.9765	29.4197	0.9790	29.3413	0.9719	29.5623
25	0.9732	29.5198	0.9762	29.4290	0.9679	29.6850
30	0.9704	29.6089	0.9736	29.5069	0.9645	29.7949
35	0.9678	29.6887	0.9714	29.5764	0.9613	29.8934
40	0.9655	29.7607	0.9694	29.6389	0.9586	29.9819
45	0.9635	29.8259	0.9676	29.6955	0.9560	30.0635
50	0.9616	29.8852	0.9660	29.7468	0.9537	30.1378

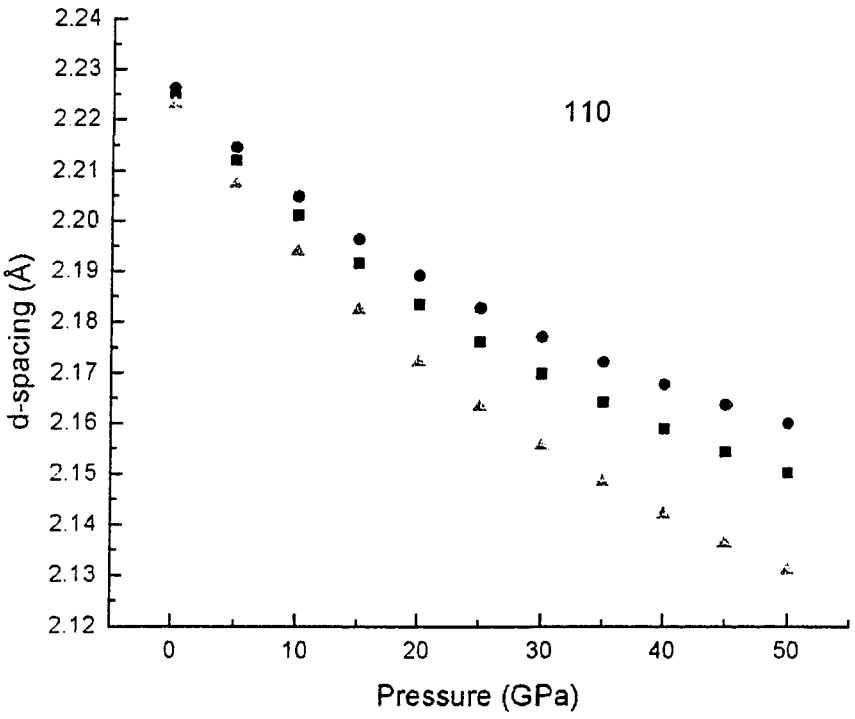

Figure 5.4 d-spacings for Mo at different points on the Debye ring (110) under different pressures. ■ stands for d-spacings under different pressures at the point where the pressure corresponds to the hydrostatic case. ● stands for d-spacings under different pressures at the point where azimuthal angle is ±90 degrees. ▲ stands for d-spacings under different pressures at the point where azimuthal angle is 0 degree.

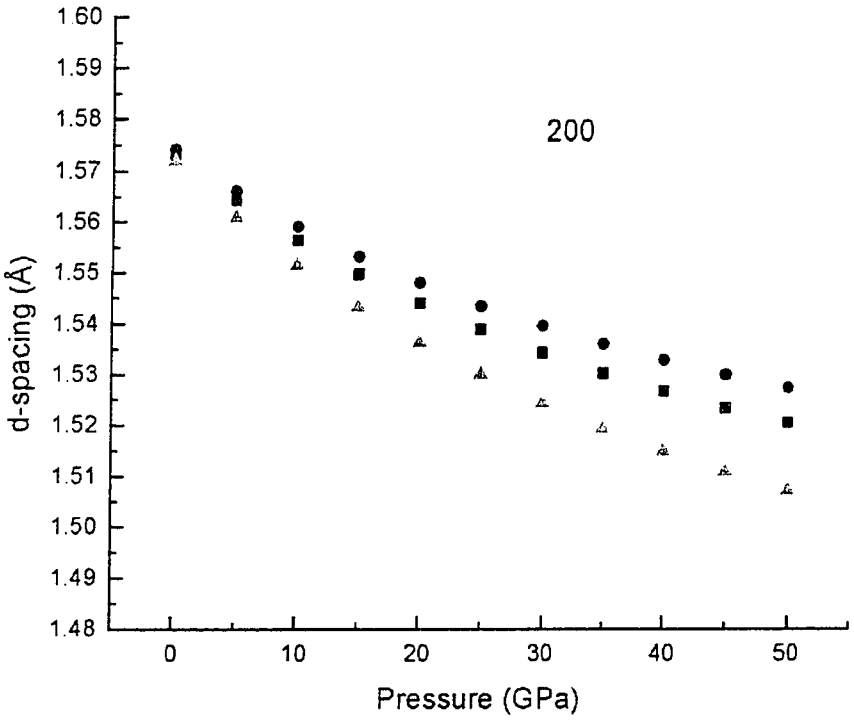

Figure 5.5 d-spacings for Mo at different points on the Debye ring (200) under different pressures. ■ stands for d-spacings under different pressures at the point where the pressure corresponds to the hydrostatic case. ● stands for d-spacings under different pressures at the point where azimuthal angle is ±90 degrees. ▲ stands for d-spacings under different pressures at the point where azimuthal angle is 0 degree.

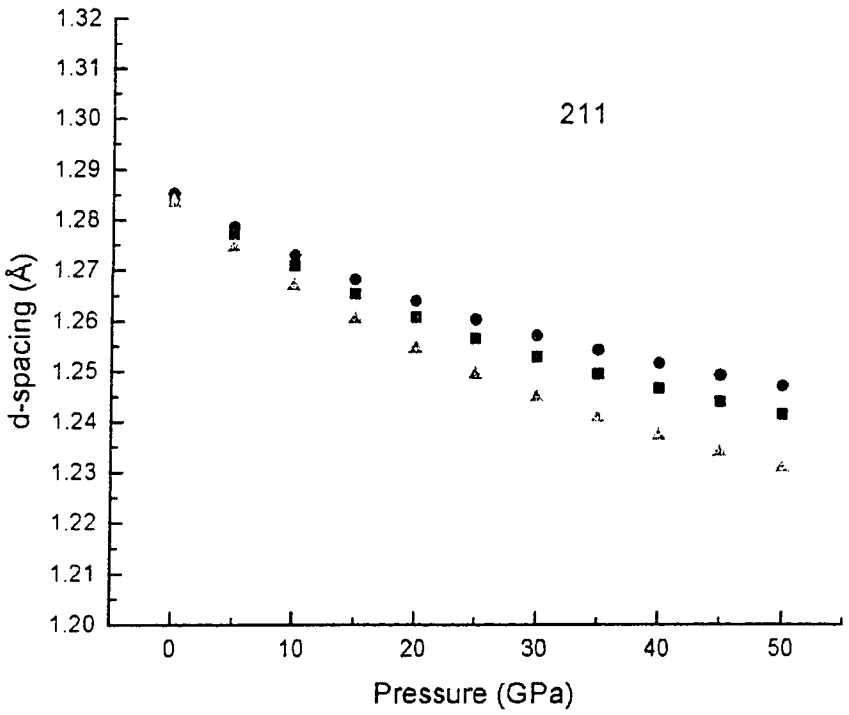

Figure 5.6 d-spacings for Mo at different points on the Debye ring (211) under different pressures. ■ stands for d-spacings under different pressures at the point where the pressure corresponds to the hydrostatic case. ● stands for d-spacings under different pressures at the point where azimuthal angle is ±90 degrees. ▲ stands for d-spacings under different pressures at the point where azimuthal angle is 0 degree.

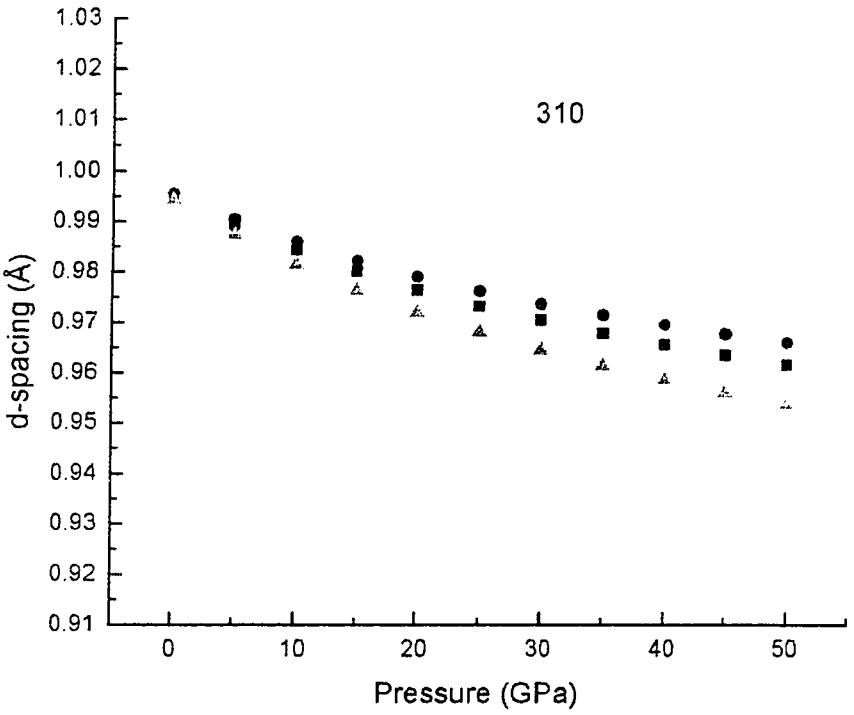

Figure 5.7 d-spacings for Mo at different points on the Debye ring (310) under different pressures. ■ stands for d-spacings under different pressures at the point where the pressure corresponds to the hydrostatic case. ● stands for d-spacings under different pressures at the point where azimuthal angle is ±90 degrees. ▲ stands for d-spacings under different pressures at the point where azimuthal angle is 0 degree.

Substituting $S_{11}(P)$, $S_{12}(P)$ and $S_{44}(P)$ into equation (4.2.10), d-spacings at different azimuthal angles are estimated. Tables 5.5, 5.6, 5.7, and 5.8 list the d-spacings and the corresponding 2θ at different azimuthal angles under 20 and 40 GPa for the diffraction lines (110), (200), (211), and (310), respectively.

Figures 5.8, 5.9, 5.10 and 5.11 illustrate the distortion in the d-spacings at different azimuthal angles under ambient pressure, 20 GPa, and 40 GPa, for the diffraction lines (110), (200), (211), and (310), respectively. The distortion of d-spacings can be seen to increase with the applied pressure. The trend of the distortion in d-spacings is in qualitative agreement with that shown in Figure 5.3.

Figure 5.12 shows the distorted Debye rings (110), (200), (211) and (310) of molybdenum under nonhydrostatic compression, in comparison to those under the corresponding hydrostatic pressure at 40 GPa. It can be seen that the Debye rings are elongated mostly at the points $\phi = 0$ and 180°, respectively, and compressed mostly at the points $\phi = 90$ and 270°, respectively (in terms of 2θ). This is again in qualitative agreement with X-ray diffraction images shown in Figures 5.2 and 5.3, as well as in agreement with other observations [21].

It can be seen as well in Figure 5.12 that the distortion in the Debye rings is very small, even at the pressure up to 40 GPa ($\Delta d/d_0 \cong 10^{-2}$). Needless to say that a high-resolution detector is critical to carry out successfully the measurements of the SCEC of a material.

Table 5.5 d-spacing and 2θ of Mo for diffraction (110) at different azimuthal angle under 20 GPa and 40 GPa, respectively. In the first column ϕ (°), azimuthal angles in degree are given. In the second and third column, d_20 (Å) and 2θ_20 (°) stand for d-spacings and X-ray diffraction angles under 20 GPa, respectively. In the fourth and fifth column, d_40 (Å) and 2θ_40 (°) stand for d-spacings and X-ray diffraction angles under 40 GPa, respectively.

ϕ (°)	d_20 (Å)	2θ_20 (°)	d_40 (Å)	2θ_40 (°)
0	2.1722	13.1088	2.1420	13.2944
5	2.1724	13.1078	2.1422	13.2934
10	2.1727	13.1058	2.1428	13.2894
15	2.1734	13.1018	2.1438	13.2834
20	2.1742	13.0968	2.1451	13.2754
25	2.1753	13.0898	2.1465	13.2664
30	2.1765	13.0828	2.1485	13.2544
35	2.1778	13.0748	2.1504	13.2424
40	2.1793	13.0658	2.1527	13.2284
45	2.1807	13.0578	2.1548	13.2154
50	2.1822	13.0488	2.1570	13.2014
55	2.1837	13.0398	2.1592	13.1884
60	2.1850	13.0318	2.1613	13.1754
65	2.1862	13.0248	2.1631	13.1644
70	2.1872	13.0188	2.1647	13.1544
75	2.1880	13.0138	2.1660	13.1464
80	2.1887	13.0098	2.1668	13.1414
85	2.1890	13.0078	2.1675	13.1374
90	2.1892	13.0068	2.1677	13.1364

Table 5.6 d-spacing and 2θ of Mo for diffraction (200) at different azimuthal angle under 20 GPa and 40 GPa, respectively. In the first column ϕ (°), azimuthal angles in degree are given. In the second and third column, d_20 (Å) and 2θ_20 (°) stand for d-spacings and X-ray diffraction angles under 20 GPa, respectively. In the fourth and fifth column, d_40 (Å) and 2θ_40 (°) stand for d-spacings and X-ray diffraction angles under 40 GPa, respectively.

ϕ (°)	d_20 (Å)	2θ_20 (°)	d_40 (Å)	2θ_40 (°)
0	1.5362	18.5774	1.5149	18.8408
5	1.5362	18.5764	1.5150	18.8388
10	1.5366	18.5724	1.5154	18.8338
15	1.5370	18.5674	1.5161	18.8258
20	1.5376	18.5604	1.5169	18.8148
25	1.5383	18.5514	1.5181	18.8008
30	1.5391	18.5414	1.5194	18.7848
35	1.5400	18.5304	1.5208	18.7668
40	1.5410	18.5184	1.5222	18.7488
45	1.5421	18.5054	1.5239	18.7288
50	1.5431	18.4934	1.5254	18.7098
55	1.5441	18.4814	1.5269	18.6908
60	1.5450	18.4704	1.5283	18.6738
65	1.5459	18.4594	1.5296	18.6578
70	1.5466	18.4514	1.5307	18.6448
75	1.5471	18.4444	1.5316	18.6338
80	1.5476	18.4384	1.5322	18.6258
85	1.5479	18.4354	1.5326	18.6208
90	1.5480	18.4344	1.5328	18.6188

Table 5.7 d-spacing and 2θ of Mo for diffraction (211) at different azimuthal angle under 20 GPa and 40 GPa, respectively. In the first column ϕ (°), azimuthal angles in degree are given. In the second and third column, d_20 (Å) and 2θ_20 (°) stand for d-spacings and X-ray diffraction angles under 20 GPa, respectively. In the fourth and fifth column, d_40 (Å) and 2θ_40 (°) stand for d-spacings and X-ray diffraction angles under 40 GPa, respectively.

ϕ (°)	d_20 (Å)	2θ_20 (°)	d_40 (Å)	2θ_40 (°)
0	1.2544	22.8009	1.2371	23.1243
5	1.2545	22.7989	1.2372	23.1223
10	1.2547	22.7949	1.2375	23.1163
15	1.2551	22.7889	1.2380	23.1063
20	1.2555	22.7799	1.2388	23.0923
25	1.2561	22.7699	1.2397	23.0753
30	1.2568	22.7569	1.2407	23.0563
35	1.2576	22.7429	1.2419	23.0343
40	1.2583	22.7289	1.2430	23.0123
45	1.2591	22.7139	1.2443	22.9883
50	1.2600	22.6979	1.2455	22.9653
55	1.2608	22.6839	1.2468	22.9423
60	1.2616	22.6699	1.2479	22.9213
65	1.2622	22.6579	1.2489	22.9023
70	1.2628	22.6469	1.2498	22.8853
75	1.2633	22.6389	1.2505	22.8723
80	1.2636	22.6319	1.2511	22.8623
85	1.2638	22.6279	1.2514	22.8563
90	1.2639	22.6269	1.2515	22.8543

Table 5.8 d-spacing and 2θ of Mo for diffraction (310) at different azimuthal angle under 20 GPa and 40 GPa, respectively. In the first column ϕ (°), azimuthal angles in degree are given. In the second and third column, d_20 (Å) and 2θ_20 (°) stand for d-spacings and X-ray diffraction angles under 20 GPa, respectively. In the fourth and fifth column, d_40 (Å) and 2θ_40 (°) stand for d-spacings and X-ray diffraction angles under 40 GPa, respectively.

ϕ (°)	d_20 (Å)	2θ_20 (°)	d_40 (Å)	2θ_40 (°)
0	0.9719	29.5623	0.9586	29.9819
5	0.9719	29.5603	0.9586	29.9799
10	0.9721	29.5553	0.9589	29.9719
15	0.9723	29.5473	0.9593	29.9589
20	0.9727	29.5363	0.9598	29.9419
25	0.9732	29.5223	0.9605	29.9199
30	0.9736	29.5073	0.9613	29.8959
35	0.9742	29.4893	0.9621	29.8689
40	0.9748	29.4703	0.9630	29.8399
45	0.9754	29.4513	0.9640	29.8099
50	0.9761	29.4323	0.9649	29.7799
55	0.9767	29.4133	0.9658	29.7509
60	0.9772	29.3963	0.9667	29.7239
65	0.9778	29.3803	0.9675	29.6999
70	0.9782	29.3673	0.9681	29.6789
75	0.9785	29.3563	0.9687	29.6619
80	0.9788	29.3483	0.9691	29.6489
85	0.9789	29.3433	0.9693	29.6419
90	0.9790	29.3413	0.9694	29.6389

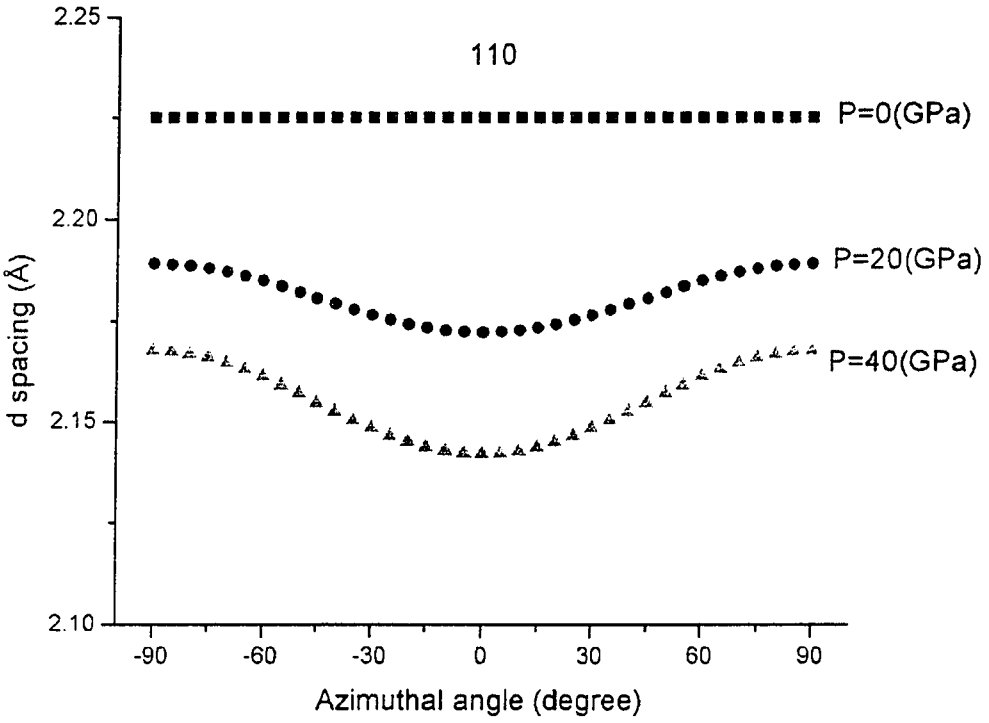

Figure 5.8 d-spacings of Mo for X-ray diffraction (110) at different azimuthal angle under ambient pressure, 20 GPa, and 40 GPa, respectively.

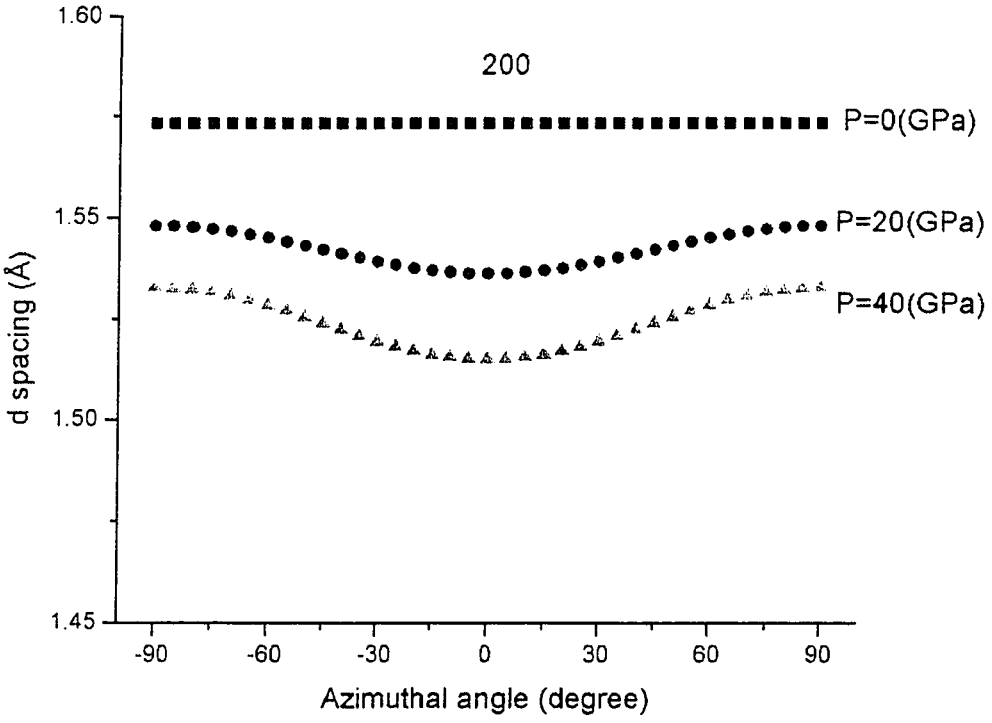

Figure 5.9 d-spacings of Mo for X-ray diffraction (200) at different azimuthal angle under ambient pressure, 20 GPa, and 40 GPa, respectively.

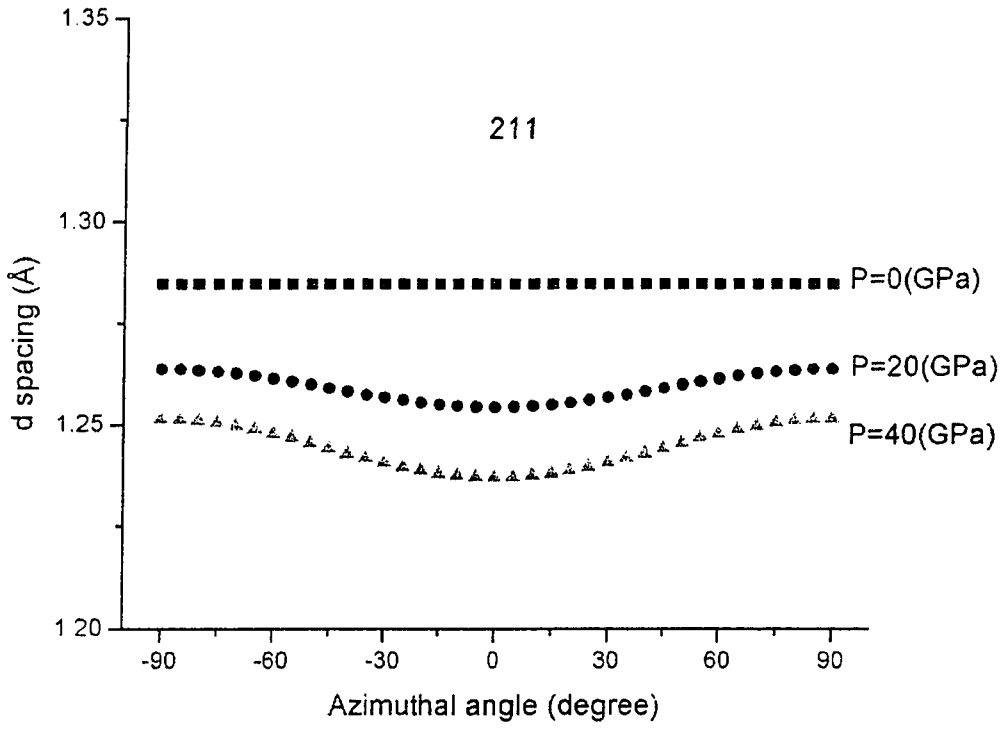

Figure 5.10 d-spacings of Mo for X-ray diffraction (211) at different azimuthal angle under ambient pressure, 20 GPa, and 40 GPa, respectively.

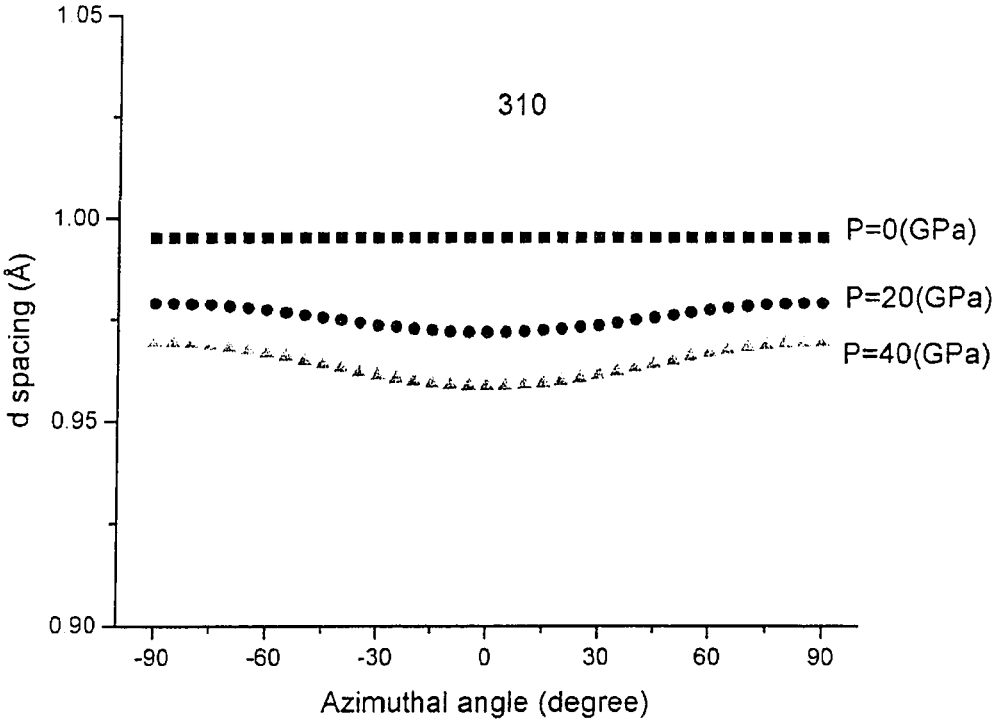

Figure 5.11 d-spacings of Mo for X-ray diffraction (310) at different azimuthal angle under ambient pressure, 20 GPa, and 40 GPa, respectively.

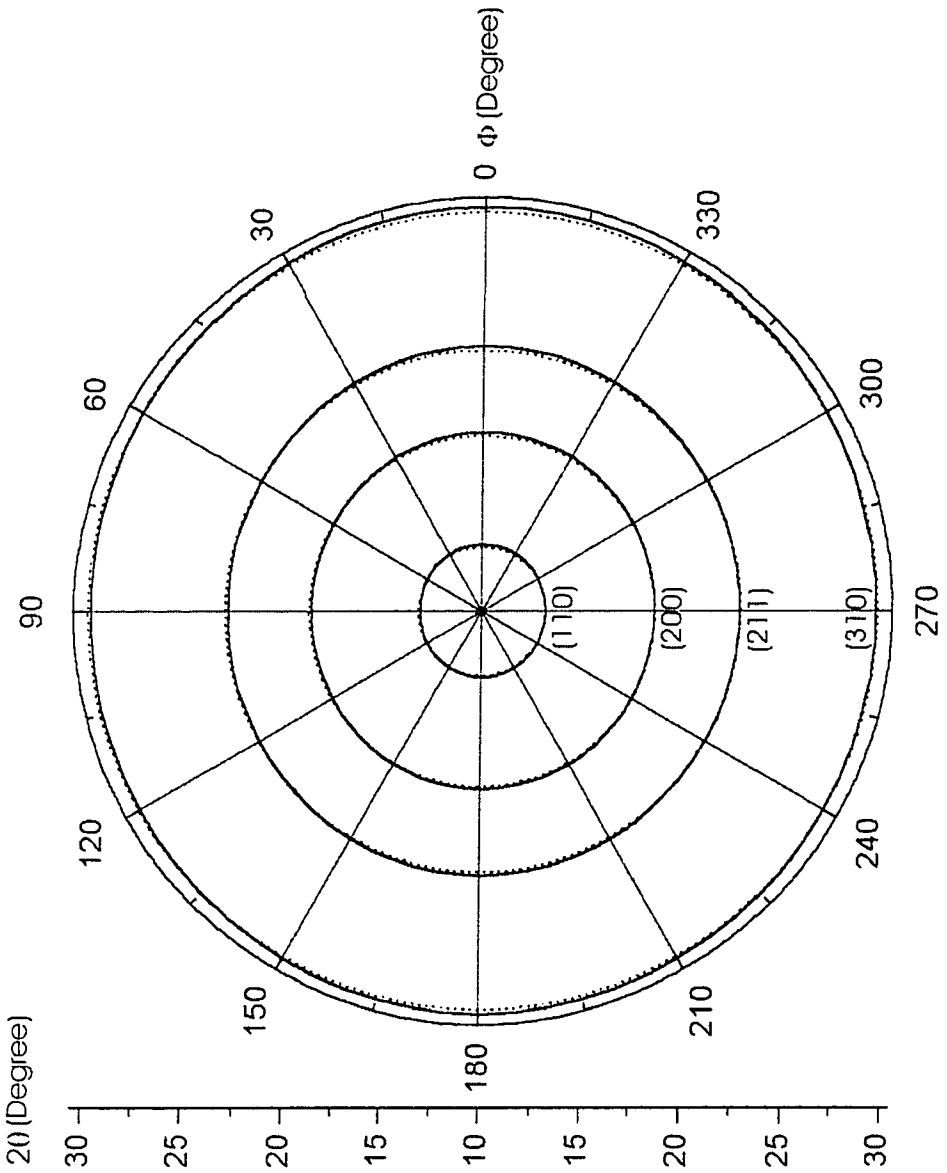

Figure 5.12 Distorted Debye rings (110), (200), (211) and (310) of Mo under nonhydrostatic compression. The corresponding hydrostatic pressure is 40 GPa. The solid lines represent those under nonhydrostatic compression. The dot lines stand for those under hydrostatic pressure.

5.3 Impact of the Relative Orientation of the Uniaxial Stress on Strains

It can be seen from Figures 5.8, 5.9, 5.10, and 5.11 that the distortion in d-spacings for all diffraction lines is dependent on the azimuthal angle. It can be seen as well from Figures 5.4, 5.5, 5.6, and 5.7 that the d-spacings at the points where the azimuthal angle ϕ equals 0° are smaller than those corresponding to the hydrostatic pressure, while the d-spacings at the points where the azimuthal angle ϕ equals angle ±90° are greater than those corresponding to the hydrostatic pressure.

The uniaxial stress component *t* experienced by all the crystallites inside the DAC is on average the same under a load, but the effect of the orientation of the uniaxial stress component *t* on the induced strain differs dramatically. Figure 5.13 illustrates the impact of the orientation of uniaxial stress component *t* on the deformation of lattice planes.

As illustrated in Figure 5.13 (A), when the uniaxial stress components *t* is perpendicular to the lattice planes (ψ equals 0°), the net force acting perpendicularly on the lattice planes is

$$\sigma_3 - \sigma_P = \frac{2}{3}(\sigma_3 - \sigma_1) > 0. \tag{5.8}$$

Therefore, the net effect is to compress the lattice planes, and the d-spacing in this case is smaller than that corresponding to hydrostatic pressure conditions.

When the uniaxial stress component t is parallel to the lattice planes (ψ equals 90°), as shown in Figure 5.13 (B), the net force acting perpendicularly on the lattice planes is

$$\sigma_1 - \sigma_p = \frac{1}{3}(\sigma_1 - \sigma_3) < 0. \tag{5.9}$$

Therefore, in this situation the net effect is to push the lattice planes aside, and the d-spacing in this case is greater than that corresponding to the hydrostatic pressure conditions.

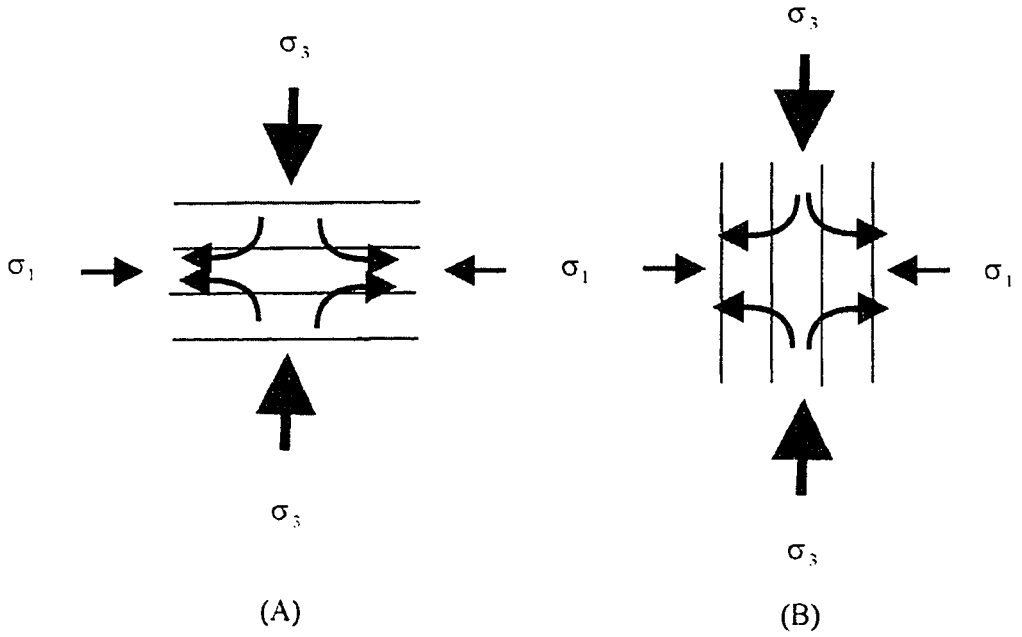

Figure 5.13 Impact of the orientation of uniaxial stress component *t* on the deformation of lattice planes. (A) The uniaxial stress component *t* is perpendicular to the lattice planes. (B) The uniaxial stress component *t* is parallel to the lattice planes.

As the azimuthal angle ϕ changes continuously from 0^o to 90^o, the orientation of the uniaxial stress components *t* changes continuously from being perpendicular to the lattice planes to being parallel to the lattice planes. Consequently the corresponding d-spacing

changes from a minimum to a maximum. In between these two values, there must be a point on a Debye ring corresponding to the value that arises from hydrostatic pressure conditions.

For the energy dispersive X-ray diffraction method, it has been noted that for ψ = 54.7°, i.e., for the situation where

$$1-3\cos^2\psi=0, \tag{5.10}$$

the d-spacings correspond to those recorded under purely hydrostatic pressure [12, 13].

For the angle dispersive X-ray diffraction method, substituting $\gamma = 90^\circ$ into equation (4.2.1), one has

$$\cos\psi_{hkl}(\phi)=\cos\phi\cos\theta_{hkl}(\phi). \tag{5.11}$$

Substituting equation (5.11) into equation (5.10), one obtains

$$1-3\cos^2\phi\cos^2\theta_{hkl}(\phi)=0. \tag{5.12}$$

Equation (5.12) is plotted as the "*x*-shaped" curve as shown in Figure 5.14. In Figure 5.14, the distorted "ellipse" plotted represents an arbitrary Debye ring recorded on an X-ray diffraction image plate, whose elongation has been deliberately exaggerated for the sake of argument. The points A, B, C and D represent the points on a Debye ring where ϕ equals 0, $\pi/2$, π and $-\pi/2$, respectively. The points H_1, H_2, H_3 and H_4, where the "*x*-shape" curve intercepts the distorted Debye ring, correspond to the situation for which purely hydrostatic pressure prevails.

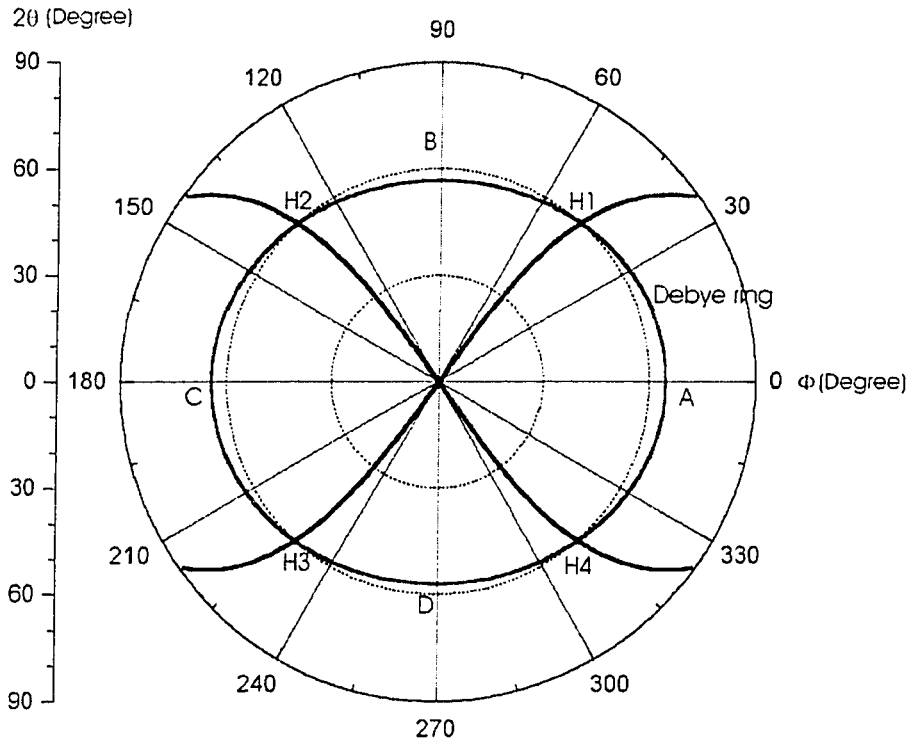

Figure 5.14 Points on a Debye ring corresponding to hydrostatic pressure condition. The "ellipse" represents an arbitrary Debye ring plotted in a polar coordinate system (2θ, ϕ). The "*x*-shaped" curve is plotted according to equation $1-3\cos^2\phi\cos^2\theta_{hkl}(\phi)=0$. Points A and C, where ϕ equals 0 and 180°, respectively, correspond to the situation for which the lattice planes are compressed maximally (in terms of d spacing) for the recorded Debye ring by the deviatoric stress; Points B and D, where ϕ equals 90 and 270°, respectively, correspond the situation for which the lattice planes are pushed aside maximally (in terms of d spacing) by the deviatoric stress. Points H_1, H_2, H_3 and H_4 correspond the situation for which the lattice planes are experiencing a purely hydrostatic pressure.

As discussed before, points A and C (where ϕ equals 0 and 180°, respectively) correspond to the situation for which the lattice planes are compressed maximally for the recorded Debye ring by the deviatoric stress; points B and D (where ϕ equals 90 and 270°, respectively) correspond to the situation for which the lattice planes are pushed aside maximally by the deviatoric stress. As illustrated in Figure 5.14, points H_1, H_2, H_3, and H_4 correspond to the situation for which the lattice planes are experiencing a purely hydrostatic pressure.

Except for the four points H_1, H_2, H_3, and H_4 on a Debye ring, all the other points correspond to the situations that the lattice planes are either compressed or stretched by the deviatoric stress. More concisely, all the points ranging from H_1 to H_4 and from H_2 to H_3 on the Debye ring correspond to the situation for which the lattice planes are compressed more or less by the deviatoric stress; all the points ranging from H_1 to H_2 and from H_3 to H_4 correspond to the situation for which the lattice planes are stretched more or less by the deviatoric stress.

Based on the discussion above, it can be seen that each point on a Debye ring corresponds to a different stress state. In other words, the angle ψ (the angle between the load axis and the diffracting plane normal) is different from point to point on a Debye ring. Therefore, the distorted Debye rings recorded under nonhydrostatic compression using the ADXD method, as noted before, provide a wealth of information on the distribution of strains and stresses, from which the SCEC of a material can be determined.

Chapter 6. Conclusions

In this work, we have developed a novel approach to measure the single crystal elastic constants (SCEC) of powder samples, using powder X-ray diffraction.

Recently, A. K. Singh and co-workers have advanced lattice strain theories, and have developed the energy dispersive X-ray diffraction (EDXD) method to measure the SCEC of powder samples. In this work, we have covered part of these theories, as well as summarizing the EDXD method. In addition, new content has been added to the previous work, and, in some cases, a different point of view has been presented.

Inspired by published works, we have undertaken to develop a novel method, using the angle dispersive X-ray diffraction (ADXD) techniques combined with an X-ray recording image plate, to determine the SCEC of polycrystalline materials. By measuring the X-ray diffraction angle 2θ at some special points along the Debye rings recorded on an X-ray diffraction image plate and using the formalism derived in this work, the SCEC of the given material can be determined from a polycrystalline sample.

Attempts to measure the SCEC of powder molybdenum sample were made. As the gasket material used in this work was not very strong, the high pressure condition necessary to induce measurable strains in the sample was not achieved. Future work will most likely produce the desired results. It must be said, however, that preliminary X-ray diffraction image of perovskite and platinum (Merkel *et al.*) are, at least qualitatively, in agreement with our calculations.

References

1. J. F. Nye, Physical Properties of Crystals (Oxford University Press, London, 1975).
2. J. P. Poirier, Introduction to the Physics of the Earth's Interior (Cambridge University Press, Cambridge, 1991).
3. D. M. Teter, Mater. Res. Soc. Bull. **23**, 1 (1998).
4. X. D. Song, and Richards, Nature (London) **382**, 221 (1996).
5. A. K. Singh, J. Appl. Phys. **73**, 4278 (1993).
6. A. K. Singh, J. Appl. Phys. **74**, 5920 (1993).
7. A. K. Singh, and C. Balasingh, J. Appl. Phys. **75**, 4956 (1994).
8. A. K. Singh, H. K. Mao, J. Shu, and R. J. Hemley, Phys. Rev. Lett. **80**, 2157 (1998).
9. A. K. Singh, and C. Balasingh, J. Appl. Phys. **83**, 7567 (1998).
10. E. H. Kisi, J. Am. Ceram. Soc. **81**, 1682 (1998).
11. C. J. Howard, and E. H. Kisi, J. Appl. Cryst. **32**, 624 (1999).
12. T. S. Duffy, G. Shen, D. L. Heinz, J. Shu, Y. Ma, H. K. Mao, R. J. Hemley, and A. K. Singh., Phys. Rev. B **60**, 15063 (1999).
13. T. S. Duffy, G. Shen, J. Shu, H. K. Mao, R. J. Hemley, and A. K. Singh, J. Appl. Phys. **86**, 6729 (1999).
14. L. Dubrovinsky, N. Dubrovinskaia, S. Saxena and T. LeBihan, Materials Science and Engineering, **A288**, 187 (2000).

15. I. Jackson, S. K. Khanna, A. Revcolevschi, and J. Berthon, J. Geophys. Res. **95**, 21671 (1990)

16. C. S. Zha, T. S. Duffy, H. K. Mao, and R.J. Hemley, Phys. Rev. B **48**, 9246 (1993).

17. R. Truell, C. Elbaum, and B. B. Chick, Ultrasonic Methods in Solid State Physics (Academic Press, New York and London, 1969).

18. I. Jackson, S. K. Khanna, A. Revcolevschi, and J. Berthon, J. Geophys. Res. **95**, 21671 (1990).

19. J. I. Langford, and D. Louër, Powder Diffraction, Rep. Prog. Phys. 59, 131 (1996).

20. A. L. Ruoff, H. Xia, and Q. Xia, Rev. Sci. Instrum. **63**, 4342 (1992).

21. L. Marques, M. Mezouar, J.–L. Hodeau, M. Núñez-Regueiro, N. R. Serebryanaya, V. A. Ivdenko, V. D. Blank, and G. A. Dubitsky, Science, **283**, 1720 (1999).

22. G. L. Kinsland and W. A. Bassett, J. Appl. Phys. **48**, 978 (1977).

23. G. L. Kinsland and W. A. Bassett, Rev. Sci. Instrum. **47**, 130 (1976).

24. F. Birch, J. Geophys. Res., **57**, 227 (1952).

25. H. K. Mao, P. M. Bell, J. W. Shaner, and D. J. Steinberg, J. Appl. Phys., 49, 3276, (1978).

26. S. Desgreniers, SimPA User Guide, technical report, LPSD/University of Ottawa, 1997 (unpublished).

27. K. Lagarec, Pressure-Induced Structural Modification in Dioxides of Group IVB Elements: TiO_2, ZrO_2 and HfO_2 (University of Ottawa, 1996).

28. A. Reuss and Z. Angew, Math. Mech. **9**, 49 (1929).

29. W. Voigt, *Lehrbuch der Kristalphysik* (Teubner, Liepzig, 1928).

30. S. Merkel, G. Montagnac, J. Badro, and P. Gillet, personal communication and ESRF User's Report, HS 1210 (2000).